5-10-2018

CFD EVALUATION OF COUNTER-FLOWING WALL JET

Sachin Sharma
University of Windsor

CFD EVALUATION OF COUNTER-FLOWING WALL JET

By

Sachin Sharma

A Thesis

Submitted to the Faculty of Graduate Studies

through the Department of Mechanical, Automotive & Materials Engineering

in Partial Fulfillment of the Requirements for

the Degree of Masters of Applied Science

at the University of Windsor

Windsor, Ontario, Canada

2018

CFD EVALUATION OF COUNTER-FLOWING WALL JET

by

Sachin Sharma

APPROVED BY:

_____

T. Bolisetti

Department of Civil and Environmental Engineering

_____

G. Rankin

Department of Mechanical, Automotive and Materials Engineering

_____

R. Balachandar, Co-Advisor

Department of Civil and Environmental Engineering

_____

R. Barron, Co-Advisor

Department of Mathematics and Statistics

May 4, 2018

DECLARATION OF CO-AUTHORSHIP/PREVIOUS PUBLICATION

I. Co-Authorship Declaration

I hereby certify that this dissertation incorporates the outcome of research undertaken under the guidance of Dr. Ram Balachandar and Dr. Ronald M. Barron from the University of Windsor. Dr. Jesudhas's contribution in this research is to the extent of providing advice in the preparation of the manuscripts catalogued in the next section. In all cases, I certify that I am the principal author and have had a major role in the preparation and writing of the manuscripts.

I am aware of the University of Windsor Senate Policy on Authorship and I certify that I have properly acknowledged the contribution of other researchers to my dissertation and have obtained written permission from each of the co-authors to include the above material in my thesis.

I declare that, with the above qualifications, this dissertation, and the research to which it refers, is the product of my own work.

II. Declaration of Previous Publications

This dissertation includes two conference papers as listed below:

Dissertation Chapter	Publication title/full citation	Publication status
Chapter 3	Sachin Sharma, Vimaldoss Jesudhas, Ram Balachandar and Ronald Barron, CSME International Congress "*Shear layer instabilities in a Counter-flowing wall jet*" York University, (May 27-30, 2018),Toronto, Canada	Accepted

I certify that the above material describes work completed during my registration as a graduate student at the University of Windsor.

III. General

I declare that, to the best of my knowledge, my thesis does not infringe up on anyone's copyright nor violate any proprietary rights and that any ideas, techniques, quotations, or any other material from the work of other people included in my thesis are fully acknowledged in accordance with the standard referencing practices. Furthermore, to the extent that I have included copyrighted material that surpasses the bounds of fair dealing within the meaning of the Canada copyright Act.

I declare that this is the true copy of my thesis, including any final revisions, as approved by my thesis committee and the Graduate Studies office,

and that this thesis has not been submitted for a higher degree to any other University or Institution.

ABSTRACT

Counter-flowing wall jets are used as mixing devices in several industrial engineering applications, for instance; mixing of effluents in rivers, enhancement of the heat transfer from the walls, etc. Although some experimental and numerical studies have been carried out to analyze the characteristics of counter-flowing wall jets, the internal turbulence structure is yet to be understood. An analysis of the dynamics of the turbulent structures would aid in the characterization of turbulent dissipation in the counter-flowing wall jet flow field. In this study, a counter-flowing wall jet issuing into a main flow is numerically investigated using a three-dimensional, unsteady, Improved Delayed Detached Eddy Simulation for a velocity ratio (jet to main flow) of 5:1. The results of the simulation are validated with available experimental data and are presented with pertinent discussions. The interaction of the jet with the wall and the main flow results in the oscillation of the stagnation point and generates significant turbulence. The feedback mechanism between the stagnation region and the shear layer of the counter-flowing wall jet is analysed by examining the instantaneous flow field. To describe the internal structure of turbulence, the coherent structures within the flow are identified using a vortex identification criterion. These structures are also quantitatively evaluated using proper orthogonal decomposition (POD). The dynamics of the organized structures reveal the complexity of the turbulence in the counter-flowing wall jet flow field.

DEDICATION

To my Parents, Dayachand Sharma and Smt. Santra Devi

ACKNOWLEDGEMENTS

TABLE OF CONTENTS

LIST OF FIGURES

NOMENCLATURE

h_j	[mm]	Jet size
U_0	[ms^{-1}]	Main flow velocity
U	[ms^{-1}]	Instantaneous streamwise velocity
N	[-]	Number of snapshots
$\mathbf{S_T}$	[-]	Strain tensor
t	[s]	Time
tke	[m^{2}s^2]	Turbulent kinetic energy
$\overline{U}$	[ms^{-1}]	Mean streamwise velocity
U_j	[ms^{-1}]	Velocity at jet exit
U_m	[ms^{-1}]	Maximum value of U
$\sqrt{\overline{u'^2}}$	[ms^{-1}]	RMS values of velocity fluctuations in x direction
u',v',w'	[ms^{-1}]	Velocity fluctuations in x, y and z directions
x,y,z	[m]	Cartesian axis directions
y^+	[-]	Wall normal distance
α	[-]	Velocity ratio (U_j/U_0)
$\lambda_1, \lambda_2, \lambda_3$	[-]	Eigenvalues of ($S_T^2 + \Omega^2$)
$\mathbf{\Omega}$	[-]	Rotational tensor
ω	[s^{-1}]	Specific dissipation rate
ω_z	[s^{-1}]	z-vorticity
TKE	[m^{2}s^2]	Mean turbulent kinetic energy
T	[s]	Time period of oscillations

Scalars

d	Distance to the nearest wall
t	Time
u^*	Reference velocity that is used in wall functions
u^+	wall-parallel velocity non-dimensionalized
G_k	turbulent production
G_ω	production of specific dissipation rate
I	turbulence intensity
L	turbulent length scale
Re_T	turbulent Reynolds number
S	strain rate parameter
V	cell volume
v	velocity magnitude
ρ	density
μ	dynamic viscosity
μ_t	turbulent viscosity
υ_t	kinematic viscosity

σ_k, σ_ω inverse turbulent Schmidt numbers

CHAPTER 1.   INTRODUCTION

1.1. Turbulent Jets

Turbulent jets are the discharge of fluid from an orifice into another large body of fluid. They are driven by the initial momentum at the orifice. Turbulent jets are encountered in various day-to-day applications and are also employed in several engineering applications such as effluent/pollutant dispersion in rivers (Lam and Chan, 1995), thrust vectoring in jet engines (Peck, 1981), etc. Fig. 1.1a depicts the discharge of effluents off the coast of Florida. The jet-like discharge and its effects on the aquatic flora and fauna is of interest to marine eco-biologists. Fig. 1.1b shows an application of a turbulent jet (marked by a black arrow) in oil piston cooling in an engine where the turbulent jet is used to enhance the heat transfer and cool the piston.

1.2. Turbulent Jet emanating into a stagnant fluid

When the jet from an orifice expands freely without any confinement it is termed as free jet. A schematic of a typical free jet flow field is shown in Fig. 1.2. As the free jet emanates from the orifice into the stagnant surrounding fluid, a shear layer is created between the jet and ambient fluid (Fig. 1.2), which is the region of high turbulence. From a flow development perspective, the typical free jet flow field can be divided into two regions: flow development region and fully developed flow region (Rajaratnam, 1976). The region from the orifice exit to $x/b_0 \approx 12$, where b_0 is width of the orifice, is termed as the flow-development region. Turbulence is confined to the edges of the jet in this region. The wedge-shaped region where the velocity is the same as the jet exit velocity ($U = U_j$) is called the potential core of the jet. Further downstream, the turbulence from

the shear layer penetrates the whole jet flow field. The velocity decreases from maximum value (U_m) at the center to zero value at some lateral distance away from the axis as shown in Fig. 1.2. When the velocity distributions at different streamwise locations collapse onto a common curve they are termed as self-similar. This region is known as the fully development region. Non-dimensional velocity (U / U_m) and length scales (y / $y_{1/2}$) are used to collapse the velocity profiles. Here U_m is the maximum streamwise velocity at any section and $y_{1/2}$ is the jet half width defined as the y location where velocity is half of the maximum velocity ($U = U_m/2$). Between the flow development region and fully developed flow region is the transition region. Here the turbulence reaches the centerline of the jet, however the velocity profiles are not self-similar.

In certain scenarios, expansion of the jet can be confined by the presence of the wall. Fig. 1.3a depicts the flow field of a typical wall jet issuing into a stagnant surrounding. As the wall jet emanates into the stagnant flow, a boundary layer is formed near the walls and a shear layer is formed on the other edge of the jet. The potential core of the wall jet is consumed when the turbulence from the boundary layer and shear layer penetrates the centerline of the jet. After the region of the potential core, the fully developed region occurs. Further downstream similar to the free jet, the velocity distributions at different streamwise locations become self-similar. The velocity field of the wall jet is divided into two regions: inner region and outer region (Lauder and Rodi, 1983) as shown in Fig. 1.3b. The inner region extends from the wall ($y = 0$) to the point of maximum velocity (y_m). The outer region is extended from the point of maximum velocity to the outer edge of the jet. The inner region has the characteristics of a boundary layer and the outer region has characteristics of a free jet. The development of the

boundary layer near the wall further enhances the turbulence in a wall jet. Extensive research has been carried out on both free and wall jets issuing into stagnant flow (Hammond, 1982; Lauder and Rodi, 1983; George et al., 2000; Tachie et al., 2002) and the velocity and turbulence characteristics are well documented.

1.3 Turbulent jets issued into a moving fluid

Turbulent jets are often issued into a moving body of fluid. This moving body of fluid into which the jet emanates is referred to as the main flow. Based on the direction of main flow with respect to the turbulent jet, the flow field can be classified as:

1.3.1   Co-flowing jets: When the jet issues from an orifice in the same direction as the main flow, it is known as a co-flowing jet (Fig. 1.4a). The flow field of a co-flowing jet is divided into strong and weak jet regions (Antonia and Bilger, 1974; Rajaratnam, 1976). The region where the centerline velocity of the jet is greater than the main flow velocity is known as the strong jet region ($U_j > U_o$); whereas the region were the centerline velocity approaches the main flow velocity is referred to as the weak jet region ($U_j < U_o$).

1.3.2   Cross-flowing jets: A cross-flowing jet is formed when the jet is issued at an angle to the main flow as shown in Fig. 1.4b. Several researchers (Andreopoulos and Rodi, 1984) have studied mean and turbulent characteristics of cross-flowing jets. These studies have revealed the complexity of the cross-flowing jet flow field.

1.3.3 Counter-flowing jets: Counter-flowing free jets (CFFJ) are formed when the free jet is issued opposite to the direction of the main flow. The schematic of counter-flowing jets is shown in Fig. 1.4c. Studies on CFFJ (Yoda and Fiedler, 1996; Lam and Chan,

3

1995) have shown that the turbulence in CFFJ is significantly higher than that occurring in co-flowing or cross-flowing jets. This has rendered counter-flowing jets ideal for several mixing and heat transfer enhancement applications in the industry. Fig. 1.4c depicts the schematic of a typical CFFJ flow field. The initial momentum at the jet exit causes it to penetrate the main flow. Gradually, the velocity of the jet decreases and becomes zero at the stagnation point (x_s). At the stagnation point, the main flow pushes against the jet, causing it to turn back, which creates the recirculation region. A unique feature of counter-flowing jets is the formation of this recirculation region. The presence of the recirculation region helps to enhance the turbulence.

1.4   Counter-flowing wall jet

Counter-flowing wall jets (CFWJ) are also often encountered. The presence of the wall in a CFWJ further enhances the turbulence, making them even more complex to analyze. Fig. 1.5 shows the schematic of a CFWJ. Similar to a CFFJ, the initial momentum of the source drives the wall jet to penetrate into the main flow up to a stagnation point, where the main flow pushes the jet in the opposite direction to create a recirculation region. The position at which the mean jet axial velocity becomes zero is defined as the stagnation point. The distance between the jet exit and the stagnation point is called the penetration length (x_s) of the wall jet. The locus of points where $U = 0$, shown in Fig. 1.5, divides the forward and backward flow. Also shown in Fig. 1.5 is the curve along which $U=U_0$. The $U=U_0$ curve starts near the stagnation point and divides the jet flow and main flow (Yoda and Fiedler, 1996). The maximum vertical distance from the bed to $U=U_0$ curve is referred to as the width of the recirculation zone (h). A comprehensive overview of the CFFJ and CFWJ literatures is presented in Chapter 3.

1.5   Motivation of the present study

The studies on CFWJ are sparse compared to co-flowing, cross-flowing or even the CFFJ. Since counter-flowing wall jets are often employed to enhance mixing and heat transfer, understanding the internal turbulence structures of CFWJ becomes important. However, the experimental and numerical studies that have been carried out to analyze the characteristics of counter-flowing wall jets have not adequately described the complete internal turbulence structure of the CFWJ flow field. Since experimental studies measure the flow quantities at specific points or planes, the complete three-dimensional flow field is not available for analysis. Also, several of the earlier numerical studies on CFWJ relied on Reynolds-Averaged Navier Stokes (RANS) to model turbulence. Since the two-equation RANS models are inherently isotropic, they are not suitable to capture the anisotropic turbulent structures in the CFWJ flow field. The objective of the present study is to address these limitations by performing a three-dimensional, unsteady numerical simulation of the CFWJ flow field using a suitable turbulence model that can capture the anisotropic structures in the flow.

1.6   Organization of the thesis

This thesis is organized into four chapters. The content of the chapters is briefly explained below:

Chapter 1 is a general introduction to turbulent jets and their classification, the motivation and objectives of the present study are also discussed

Chapter 2 presents a brief overview of the turbulence modelling approaches. The advantages of a hybrid RANS-Large Eddy Simulation (LES) approach to model

turbulence is highlighted. The present study uses the improved Delayed Detached Eddy Simulations (IDDES) approach to model turbulence. The formulation of this model is also presented.

Chapter 3 presents the flow field of the counter-flowing wall jet. The simulation setup details are presented along with the details of the mesh. The simulation results are validated with the experimental results of Tudor (2003) and other available experimental data. The mean quantities, including velocity, Reynolds stresses and vorticity, are presented with detailed discussion. The coherent structures are educed using both the λ_2-criteria and proper orthogonal decomposition (POD). The internal turbulence structure of the counter-flowing wall jet flow field is described by analyzing the dynamics of the organized structures in the flow.

The summary and conclusions are presented in Chapter 4 along with recommendations for future work.

Fig. 1.1 (a) Image of the turbulent jet used as effluents mixing in a river (b) oil squirter

assembly for piston cooling

7
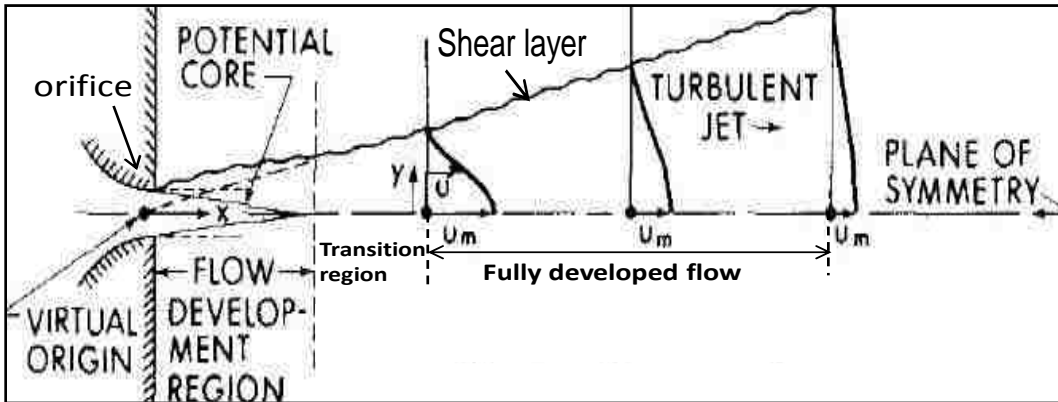
Fig.1.2 Typical flow field of plane free jet issuing into stagnant ambient fluid (adapted

from Rajaratnam, 1976)
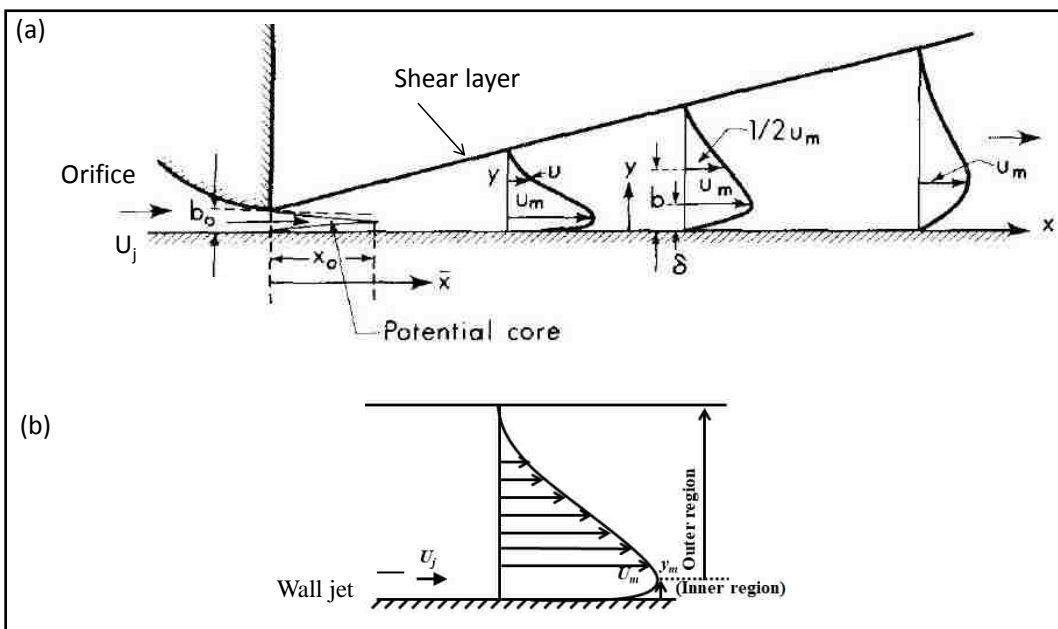
Fig. 1.3 (a) Typical flow field of plane wall jet issuing into stagnant ambient fluid

(adapted from Rajaratnam, 1976), (b) velocity profiles of wall jet at any section
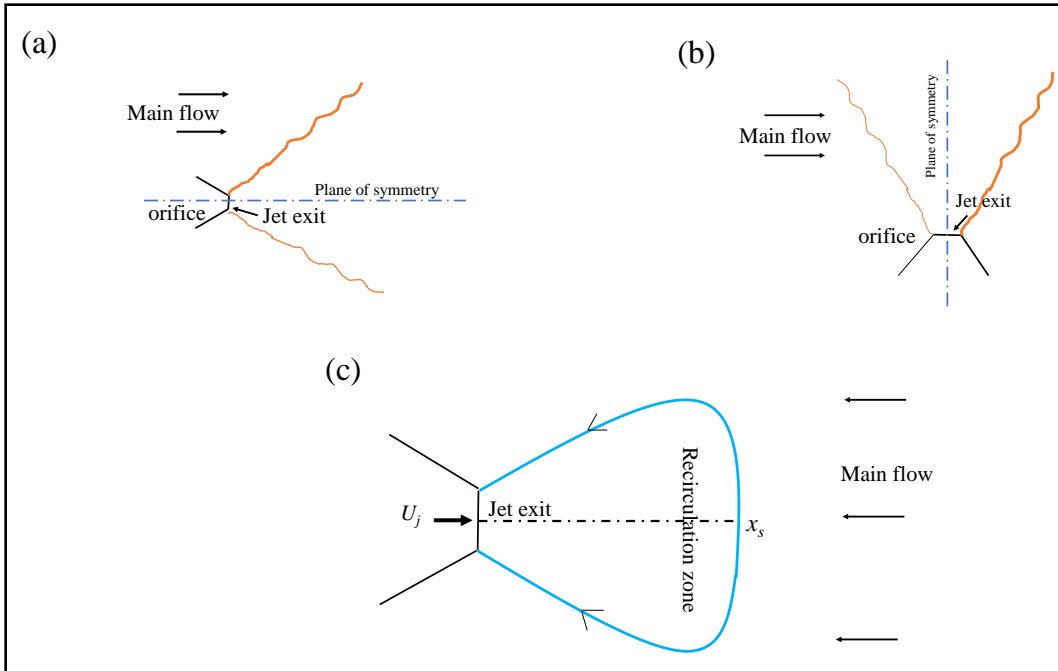
Fig. 1.4 (a) Co-flowing jets, (b) Cross-flowing jets, (c) Counter-flowing jets
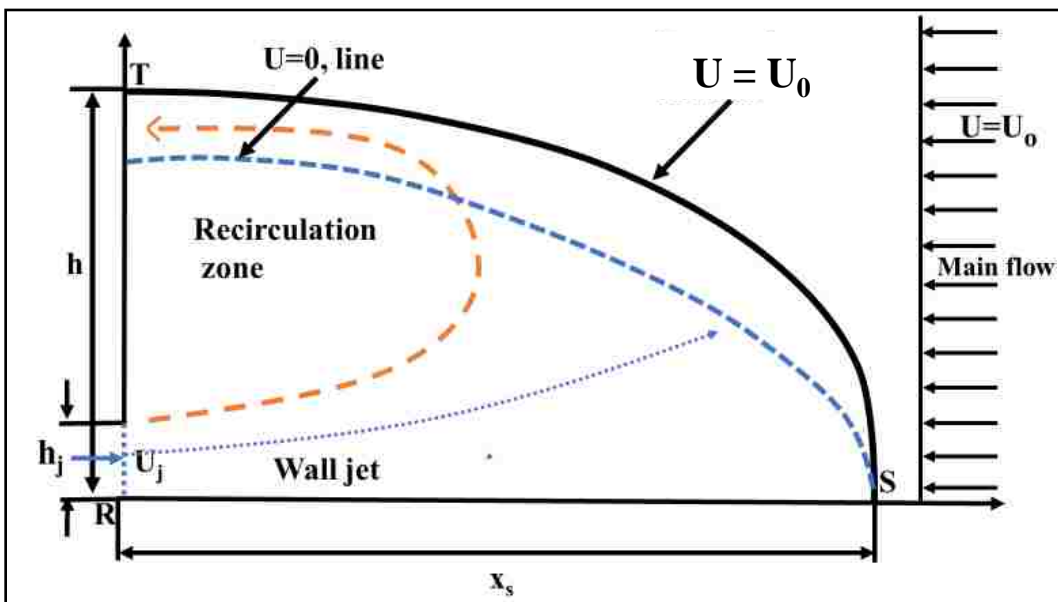
Fig. 1.5 Schematic of counter-flowing wall jet

CHAPTER 2. TURBULENCE MODELLING

2.1. Introduction

In this chapter, various turbulence modelling approaches relevant to this thesis are briefly discussed. The present simulation uses a hybrid RANS-LES approach known as Improved Delayed Detached Eddy Simulation (IDDES). The simulation is carried out using the commercial code STAR-CCM+. This solver uses the finite volume approach to discretize the governing Navier-Stokes equations. This code is well suited in handling complicated flow problems (Jesudhas et al., 2018), complex geometries (Nasif et al., 2014), etc. The complete formulation for IDDES is presented based on the equations from STAR-CCM+ User Guide v10.06.010 and Shur et al., (2008).

2.2. Turbulence modelling approaches

Modelling turbulence is the subject of ongoing intensive research over the last 50 years. The complexity of modelling turbulence arises from the different scales of the flow that must be resolved. The different approaches that are conventionally used are described below:

2.2.1 Reynolds-Averaged Navier-Stokes turbulence model

Reynolds-Averaged Navier-Stokes (RANS) model solves the time-averaged Navier Stokes equations. The flow variables in the governing equations are replaced by the mean and fluctuating components (Reynolds decomposition). RANS resolves the mean quantities and models the turbulence quantities, leading to moderate computational cost. However, two-equation RANS models are inherently isotropic, which is not an ideal

assumption in a flow field where large-scale anisotropic unsteady vortical structures are present, such as in the wake region behind bluff bodies (Frohlich and von Terzi, 2008).

2.2.2. Large Eddy Simulation

Large Eddy Simulation (LES) resolves the large-scale eddies by solving the Navier-Stokes equations and the small-scale eddies are modelled using sub-grid scale models (SGS). LES works on the spatial filtering approach. LES is best suited to model the anisotropic turbulence. However, LES is significantly more computationally expensive than RANS (Frohlich and von Terzi, 2008).

In wall bounded flows, the small-scale structures are found near the walls, resulting in the need for a very fine grid near the wall for LES. This becomes impractical for high Reynolds number applications, since LES requires that the grid size be reduced as the Reynolds number increases. To avoid this shortcoming, RANS can be used near the walls and LES away from them. This type of approach is known as the hybrid RANS-LES approach.

2.3. Hybrid RANS- LES approach

Spalart et al. (1997) proposed a hybrid RANS-LES approach known as Detached Eddy Simulation (DES), which uses RANS near the walls and LES away from the walls. The switch from RANS to LES regions was based on the mesh size. However, the log-layer predicted by the RANS model and the LES model did not match in the near-wall region, resulting in under-predicting the skin-friction coefficient (Shur et al., 2008). To alleviate this shortcoming, Shur et al. (2008) proposed IDDES. IDDES defines a new sub-grid length scale that not only depends on the grid size but also on the wall normal distance. It

ensures a delay in the switching of RANS to LES in the near-wall region and thereby avoids the "log-law" mismatch error.

In the present study, the k-ω shear stress transport (SST) RANS model is used due to its ability to handle the presence of adverse pressure gradient in the CFWJ flow (Menter, 1992). This is combined with LES, and IDDES is used to model the turbulence. The formulation of the k-ω shear stress transport (SST) model is discussed in the next section.

2.4. Shear Stress Transport k-ω Model

Basic Transport Equations

The transport equations for the SST k-ω model are (Versteeg and Malalasekera, 2007; STAR-CCM+ User Guide v10.06.010) given as:

$$\frac{d}{dt}\int_V \rho k dV + \int_A \rho u k.\boldsymbol{n} da = \int_A \left(\mu+\sigma_k\mu_t\right)\nabla k \cdot \boldsymbol{n} da + \int_V \left(G_k- \rho\beta^* f_{\beta^*}(\omega k-\omega_0 k_0)+S_k\right) dV \qquad (1)$$

$$\frac{d}{dt}\int_V \rho\omega dV + \int_A \rho\omega u \cdot \boldsymbol{n} da = \int_A \left(\mu+\sigma_\omega\mu_t\right)\nabla\omega \cdot \boldsymbol{n} da + \int_V \left(G_\omega-\rho\beta f_\beta(\omega^2-\omega_0^2)+D_\omega+S_\omega\right) dV \quad (2)$$

where k is the turbulent kinetic energy, ω is the specific dissipation, S_k and S_ω are user-specified source terms, k_0 and ω_0 are the ambient turbulence values, G_k is the turbulent production, G_ω is the production of the dissipation rate, μ is dynamic viscosity, μ_t is the turbulent viscosity, σ_k and σ_ω are turbulent Schmidt numbers, and

$\beta^* = 0.09$.

Turbulent Production

The production of turbulence G_k is evaluated as

$$G_k = \mu_t f_c S^2 - \frac{2}{3}\rho k \nabla \cdot \boldsymbol{u} - \frac{2}{3}\mu_t (\nabla \cdot \boldsymbol{u})^2 \tag{3}$$

where f_c is the curvature correction factor usually associated with streamline curvature and $\nabla \cdot \boldsymbol{u}$ is the velocity divergence and S is the modulus of the mean strain rate tensor:

$$S = |\mathbf{S}| = \sqrt{2\mathbf{S}\colon \mathbf{S}^T} = \sqrt{2\mathbf{S}\colon \mathbf{S}} \tag{4}$$

where

$$\mathbf{S} = \frac{1}{2}(\nabla \boldsymbol{u} + \nabla \boldsymbol{u}^T) \tag{5}$$

and ":" is the inner dot product of the two tensors.

The production of ω is evaluated as

$$G_\omega = \rho \gamma \left[\left(S^2 - \frac{2}{3}(\nabla \cdot \boldsymbol{u})^2 \right) \frac{2}{3}\omega \nabla \cdot \boldsymbol{u} \right] \tag{6}$$

where γ is a blended coefficient of the model.

Cross-Derivative

D_ω is a cross-derivative term, given as

$$D_\omega = 2(1-F_1)\rho \sigma_{\omega 2}\frac{1}{\omega}\nabla k \cdot \nabla \omega \tag{7}$$

where $\sigma_{\omega 2}$ is a constant with value as 0.856.

$$F_1 = \tanh(\text{arg}_1^{4}) \tag{8}$$

$$\text{arg}_1 = \min \left(\max \left(\frac{\sqrt{k}}{0.09\omega d}, \frac{500\upsilon}{d^2\omega} \right), \frac{2k}{d^2 CD_{k\omega}} \right)$$

where d is the distance to the nearest wall, υ is the kinematic viscosity and F_1 is the blending function. In this expression $CD_{k\omega}$ is related to the cross-diffusion term, defined by

$$CD_{k\omega} = \max \left(\frac{1}{\omega}\nabla k \cdot \nabla \omega, \ 10^{-20} \right) \tag{9}$$

Relation for Turbulent Viscosity

The turbulent viscosity is computed as

$$\mu_t = \rho k T \tag{10}$$

Here T is the turbulent length scale defined by Durbin (1996) as $\min\left(\frac{\alpha^*}{\omega}, \frac{a_1}{SF_{2n}}\right)$

where the model constants are taken as $a_1 = 0.31$ and $\alpha^* = 1$.

The function F_{2n} is given by

$$F_{2n} = \tanh\left(\arg_2{}^2\right) \tag{11}$$

where

$$\arg_2 = \max\left(\frac{2\sqrt{k}}{\beta^* \omega d}, \frac{500 v}{d^2 \omega}\right). \tag{12}$$

Model Coefficients

The coefficients in the model are calculated from the blending function F_1, such that each coefficient is given by

$$\phi = F_1 \phi_1 + (1-F_1)\phi_2 \tag{13}$$

The coefficients for ϕ_1 are:

$$\beta_1 = 0.0750,\ \sigma_{k1} = 0.85,\ \sigma_{\omega1} = 0.5,\ \kappa = 0.41,\ \gamma_1 = \frac{\beta_1}{\beta^*} - \sigma_{\omega1}\frac{\kappa^2}{\sqrt{\beta^*}} \tag{14}$$

The coefficients for ϕ_2 are:

$$\beta_2 = 0.0828,\ \sigma_{k2} = 1.0,\ \sigma_{\omega2} = 0.856,\ \kappa = 0.41,\ \gamma_2 = \frac{\beta_2}{\beta^*} - \sigma_{\omega2}\frac{\kappa^2}{\sqrt{\beta^*}} \tag{15}$$

In both cases, $\beta^* = 0.09$, $\alpha^* = 1$.

2.5. IDDES Formulation

For the IDDES formulation, the length scale in the dissipation term in the transport equation for k is replaced with a hybrid length scale as follows:

$$D_k = \frac{\rho k^{3/2}}{l_{\text{HYBRID}}} \tag{16}$$

Where:

$$l_{\text{HYBRID}} = f_d(1+f_e)l_t + (1+f_d)C_{\text{des}}\Delta_{\text{IDDES}}$$

Two more functions are introduced in the length scale calculation to add wall-modeled LES (WMLES) capability, a blending function f_B and an "elevating" function f_e:

$$f_B = \min[2\exp(-9\alpha^{*2}),\ 1.0] \tag{17}$$

$$\alpha^* = 0.25 - \frac{d}{\Delta} \tag{18}$$

Equation 18 represents the improvement in IDDES where the length scale is dependent on both the grid and wall normal distance (d). Other functions in l_{HYBRID} are given by

$$f_e = \max[(f_{e1}-1),\ 0]\ \psi f_{e2} \tag{19}$$

$$f_{e1} = \begin{cases} 2\exp(-11.09\alpha^{*2}) & \text{if } \alpha^* \geq 0 \\ 2\exp(-9.0\alpha^{*2}) & \text{if } \alpha^* < 0 \end{cases} \tag{20}$$

$$f_{e2} = 1.0 - \max(f_t, f_l) \tag{21}$$

$$f_t = \tanh\left[(C_t^2 r_{dt})^3\right] \tag{22}$$

$$f_l = \tanh\left[\left(C_l^2 r_{dl}\right)^{10}\right] \tag{23}$$

$$r_{dt} = \frac{v_t}{\sqrt{\nabla\mathbf{v}:\nabla\mathbf{v}^T}\kappa^2 d^2} \tag{24}$$

$$r_{dl} = \frac{v}{\sqrt{\nabla\mathbf{v}:\nabla\mathbf{v}^T}\kappa^2 d^2} \tag{25}$$

C_t and C_l are model constants, v_t is the kinematic turbulent viscosity and κ is the von Karman constant.

The WMLES and DDES branches of the model are combined using a modified version of the DDES f_d function as follows:

$$f_d = max\left(\left(1\text{-}f_{dt}\right), f_B\right) \tag{26}$$

$$f_{dt} = 1 - \tanh[(C_{dt}r_{dt})^3] \tag{27}$$

where C_{dt} is a model constant.

The IDDES model also uses an altered version of the mesh length scale Δ_{IDDES}, defined as

$$\Delta_{IDDES} = min(max(0.15*d, 0.15*\Delta, \Delta_{min}), \Delta) \tag{28}$$

where Δ_{min} is the smallest distance between the cell center under consideration and the cell centers of the neighboring cells.

2.6. Concluding Remarks

This chapter illustrates the formulation of the SST k-ω and IDDES turbulence models. The IDDES uses RANS near the walls and LES away from the walls. The blending function is monitored to ensure that the LES is activated in the region of interest (recirculation region). IDDES model is ideal to model the counter-flowing wall jet since the predominant mechanism of turbulence generation occurs inside the recirculation region.

CHAPTER 3. IDDES EVALUATION OF A COUNTER-FLOWING WALL JET

3.1   Introduction

In this chapter, a counter-flowing wall jet issuing into a main flow is numerically examined using a three-dimensional, unsteady, Improved Delayed Detached Eddy Simulation. The results of the simulation are validated with experimental results and are presented with pertinent discussions. Although some experimental and numerical studies have been carried out to analyze the characteristics of counter-flowing wall jets, the internal turbulence structure is yet to be understood. The interaction of the jet with the wall and the main flow leads to oscillation of the location of the stagnation point and generates significant turbulence. The feedback mechanism between the stagnation region and the shear layer of the counter-flowing wall jet is analysed by examining the instantaneous flow field. To describe the internal structure of turbulence, the coherent structures within the flow are identified using a vortex identification criterion. These structures are also quantitatively evaluated using POD. The dynamics of the organized structures reveal the complexity of the turbulence in the counter-flowing wall jet flow field.

Counter-flowing jets are characterized by having the jet flow opposite to the direction of the main flow. They are encountered in several engineering applications for the effective dilution of contaminants in streams (Beltaos and Rajaratnam, 1973), rapid pollutant dispersion (Lam and Chan, 1995), thrust vectoring in jet engines (Peck, 1981), etc. Turbulence in counter-flowing jets is enhanced compared to a jet flowing into a stagnant ambient flow or that occurring in co-flowing and cross-flowing jets, making

them ideally suited for mixing and combustion applications (Yoda and Fiedler, 1996). However, the enhanced turbulence also makes the flow field more complex. A detailed description of the internal turbulence structure of counter-flowing jets will assist in bringing forth the dominant physical mechanisms responsible for this complexity. Typically, a counter-flowing jet can either be a CFFJ or a CFWJ. The presence of the wall in the CFWJ further enhances the complexity of the flow field. While several experimental studies (Beltaos and Rajaratnam, 1976; Morgan et al., 1976; Lam and Chan, 1997; Yoda and Fiedler, 1996; Bernero and Fiedler, 2000) have been conducted on CFFJ, the studies on CFWJ are relatively limited. However, the existing literature on CFFJ can be used to understand the qualitative features of a CFWJ. The flow physics and shortcomings of the available studies are briefly reviewed below.

Morgan et al. (1976) studied the characteristics of a round CFFJ and measured the penetration length of the jet using dye-visualization. For a low momentum flux ratio of 0.25, they reported a linear relationship $x_s/d_j = 2.5\alpha$ between the penetration length and the velocity ratio ($\alpha = U_j/U_o$, where U_j is the velocity at the nozzle exit and U_o is the main flow velocity). Here, x_s is the penetration length (see Fig. 3.1a for definition) and d_j is the diameter of the jet. For high momentum flux ratio, the penetration length increases with α but not linearly and with a lower slope. Yoda and Fiedler (1996) studied CFFJ using planar laser-induced fluorescence (PLIF) to understand the stability characteristics at various values of α between 1.6 - 10. Their results showed that for $\alpha <$ 1.4, the flow appeared to be stable with less fluctuations in both the axial and radial directions. This translates into a smaller penetration length as the jet momentum is not sufficient to penetrate a larger distance into the main flow. For $\alpha > 1.4$, the flow was

19

unstable with significant fluctuations which contributed to a larger penetration length and a greater radial spread of the jet. They also reported that x_s is directly proportional to α. Lam and Chan (1997) conducted an experimental analysis of CFFJ using PLIF for α between 2 to 15. They found that x_s and lateral spreading of the jet increased with increasing α. Also, large temporal and spatial fluctuations were observed near the stagnation point. The maximum instantaneous fluctuations of the penetration length and lateral spreading exceeded 30% and 100% of their mean values, respectively. However, the physical processes responsible for these fluctuations need to be evaluated. Bernero and Fiedler (2000) analyzed CFFJ using laser Doppler anemometer (LDA) and PLIF for $\alpha = 1.3$ and $\alpha = 3.4$. They analyzed the coherent structures in the flow field using POD. They found that for $\alpha = 3.4$, the first mode shows the radial flapping of the jet while the second mode shows the periodic oscillations in the penetration length. Furthermore, they reported that there are several different frequencies that are present in the flow field which makes this flow field difficult to understand. In addition, they found that the first 20 modes are required for reconstructing 70% of the energy in the flow. However, for a typical jet flow in stagnant conditions, usually the first 20 modes contribute to 97% of the energy in the flow. They concluded that the flow field of CFFJ is very complex and require larger number of modes to represent the whole flow phenomenon.

Tsunoda and Saruta (2003) conducted an experimental analysis of CFFJ using PIV and PLIF. They measured the velocity and concentration fields using for values of α = 2.9, 4.0 and 5.1. As α increases, the penetration length increases but the lateral extent of the jet spread decreases. They confirmed that the velocity decay in CFFJ is faster than a jet in quiescent flow. Further, they reported the presence of two peaks in the centreline

turbulent intensity profiles which were found to be independent of α. The first peak was related to instability in the jet and the second peak was present near the stagnation region. Sivapragasam et al. (2009) numerically studied the CFFJ issuing into a confined circular duct of diameter D. The computations were performed for varying jet diameters and velocity ratios. They used the standard k-ε Reynolds-Averaged Navier Stokes (RANS) model to simulate the turbulent flow field. They concluded that the duct walls have a significant effect on the penetration length of jet. If the jet was confined in the duct, the penetration length decreased. They also confirmed the presence of two peaks in the centreline turbulent intensities.

Li et al. (2013) studied a round CFFJ using Large Eddy Simulation (LES) for α between 3 and 15, and analyzed the coherent structures in the flow field using λ_2 - criterion. They were able to identify the vortical structures that were responsible for the streamwise and radial oscillations of the round CFFJ. They reported that vortex rings appear near the jet exit in the shear layer. These vortex rings decay faster than those which form in stagnant surroundings. Furthermore, large-scale vortical structures were identified near the stagnation point. These structures pair up, break down and enable the jet to oscillate strongly with respect to its axis in this region. Li et al. (2015) also studied non-circular (square and elliptical) CFFJ using the RANS k-ε turbulence model. The simulation was carried out for α ranging from 2.2 to 10. They established that due to the higher instabilities in the non-circular jets, the entrainment of ambient fluid was significantly higher than a counter-flowing free round jet. But further downstream, the difference between the circular and non-circular jets was found to be minimal as both the square and the elliptical jets tend to become circular in cross-section with increasing

streamwise distance. Also, the instabilities in the square jet were larger than those in the elliptical jet which results in a higher value of the turbulent kinetic energy.

A common application of a counter-flowing wall jet (CFWJ) is to enhance the heat transfer from the wall (Volchkov et al., 1995). Wall-jet flow is a two-layer shear flow displaying boundary layer characteristics close to the wall and the features of a shear layer away from the wall. Fig. 3.1a shows the schematic of a typical CFWJ flow field, wherein U_j is the velocity at the nozzle exit emanating counter to the main flow with a velocity (U_o). The initial momentum of wall jet causes it to penetrate the main flow up to the stagnation point (marked by point S in Fig. 3.1a). At the stagnation point, the wall jet losses its momentum and the axial velocity of wall jet (U) becomes zero. As it loses momentum, it is pushed in the opposite direction by the main flow, creating the recirculation region. The turbulence generation and dissipation in the recirculation region stipulates the mixing. Also marked in Fig. 3.1a is the $U = U_o$ curve, which starts near the stagnation point and divides the regions influenced by the jet flow and the main flow (Yoda and Fiedler, 1996). The maximum vertical distance from the bed to $U = U_o$ line, is termed as the width of the recirculation region (h). A typical velocity profile of CFWJ within the recirculation region (section a-a) is shown in Fig. 3.1b. Similar to a typical wall jet, the inner region extends from the wall at $y = 0$ to $y = y_m$, where the velocity is maximum ($U = U_m$). The recirculation region stretches from the point of maximum velocity to the y-location where $U = U_o$. The outer region extends above the recirculation region.

Balachandar et al. (1992) conducted an experimental study on CFWJ to measure parameters such as x_s and h using dye visualization. They showed that for low velocity

ratio ($\alpha < 1.4$), the width of recirculation region was larger than the mean penetration length of the jet. For higher velocity ratios ($\alpha > 3.3$), both the x_s and h were similar in magnitude. Tanaka et al. (1994) performed an experimental study of CFWJ in a wind tunnel using hot-wire anemometry to study the turbulence characteristics. The Reynolds number based on the jet velocity was varied between 6500 to 19,500. The measurements were carried out for α between 1 and 3. They observed two distinct flow patterns. For $\alpha < 1.6$, the jet separated from the wall region at a very short distance from the nozzle exit forming a stagnation point close to the nozzle exit and for $\alpha > 2$, the wall jet penetrated deeper in to the main flow.

Tudor (2003) used LDV to measure the velocity and turbulence characteristics in the central plane of CFWJ for different values of α. They concluded that compared to a wall jet, the rate of expansion of a CFWJ was higher, which promotes rapid and efficient mixing. An empirical correlation was also developed to calculate the penetration length of CFWJ for varying α. Barata et al. (2009) studied CFWJ in a wind tunnel. They used LDV to measure the velocity and turbulence characteristics. They reported a small recirculation region downstream of the stagnation point created by the reversal of the jet and the main flow boundary layer, which contributes to the fluctuations near the stagnation point. Mahmoudi and Fleck (2017) studied the round CFWJ and measured the mean and turbulent characteristics using particle image velocimetry for α between 2.5 to 25 and varying Reynolds numbers (1000 – 10,000). They concluded that the decay rate of the mean axial velocity of the CFWJ was similar to a wall jet up to an axial distance of $0.7\,x_s$. Because of the occurrence of an increased lateral spreading in the round CFWJ, the penetration length was less than a planar CFWJ. Furthermore, they concluded that

because of wall effects, the amplitude of fluctuations in the penetration length of CFWJ was less than the CFFJ.

Despite the aforementioned experimental studies on CFWJ, its complete internal turbulence structure is yet to be fully understood. While experimental studies analyzed the important flow variables at specific points or planes, the complete three-dimensional flow field is not available for analysis. Also, conventional experimental devices have shortcomings when measuring close to the bed. To address these limitations and to identify the coherent structures responsible for the enhanced turbulent transport in a CFWJ, the present computational study is carried out. In this study, a three-dimensional, unsteady, IDDES is performed. The velocity and turbulence parameters are validated using available experimental data. The coherent structures in the flow were identified using the λ_2 criteria. Quantitative analysis of the organized structures is carried out using POD.

3.2   The Model

The present study adopts a hybrid RANS-LES approach to model the turbulent flow field. This is done to reduce the computational cost, retain the ability to simulate the anisotropic vortical structures efficiently in regions of interest and to combine advantages of both the RANS and the LES modelling approaches. Shur et al. (2008) proposed the IDDES, which ensures a delayed switching of RANS to LES near the walls, thereby avoiding the log law mismatch error seen in the original DES formulation. For the RANS portion, the k-ω shear stress transport (SST) model is used as it tends to perform better where adverse pressure gradients are present in the flow (Menter, 1992). The complete formulation of IDDES is described in several publications (Shur et al. 2008; Jesudhas

2016) and not repeated here for brevity. The present simulation was carried out using the commercial CFD software STAR-CCM+ v10.06.

The computational domain is modelled based on the experiments of Tudor (2003) to enable a direct comparison for validation of results. The 3D computational domain is 2.5 m x 0.24 m x 1.21 m. The central plain of the domain is shown in Fig. 3.2a. The Cartesian coordinates x, y, and z are adopted as streamwise, vertical (bed normal) and transverse directions, respectively. The height of the jet nozzle exit is 12.7 mm. The boundary conditions used in the simulation are also shown in Fig. 3.2a. The no-slip boundary condition is used on the sidewalls of the domain. At the nozzle exit, a uniform velocity of $U_j = 0.73$ m/s is provided. A uniform velocity of 0.14 m/s is provided at the entrance to the main flow. A portion of the computational mesh in the central plane is shown in Fig. 3.2b. Grid refinements are made in the regions of interest (A and B) as shown in Fig. 3.2b. Region A, in Fig. 3.2b, consists of the inner region and shear layer and B depicts the recirculation region. A total of six prism layers were used near the walls to resolve the wall effects. The value of y^+ (y^+ is a non-dimensional wall normal distance), is higher near the nozzle exit and it decreases as jet progress further downstream. Since the value of y^+, varies in the streamwise direction due to the decay of the CFWJ, all-y^+ treatment available in STAR-CCM+ is used. Based on a grid independency study, the mesh selected for the present simulation consists of about 10 million hexahedral cells. IDDES uses a blending function to switch between RANS and LES models. The value of blending function is 1 in the RANS region and 0 in the LES region (STAR-CCM+ v10.06 user guide). The blending function was monitored to ensure that LES was used in the region of interest (recirculation region). The solution is

considered to be converged when the normalized residuals fell below 10^{-6}. The unsteady simulations were run with a time step of 1 ms. The mean quantities discussed herein are obtained by averaging the data for a time period of 50 s following convergence. Longer time periods were also considered to ensure that the mean results didn't change beyond averaging the data more than 50 s.

3.3 Validation

The validation procedure adopted was based on the American Institute of Aeronautics and Astronautics (AIAA) guide lines for verification and validation of CFD simulations (2002). These guidelines encourage a 'building block' approach to validation. The CFD solver must be validated for several subsystem cases representing sub-physics for which the data is available. The IDDES model has been extensively validated for flows with strong shear layers, jets, wakes and wall-jet type flows (Nasif et al., 2014; Jesudhas et al., 2016; Jesudhas et al., 2018). Hence, the present validation procedure will focus on the validation of the present CFWJ simulation.

Fig. 3.3a depicts the variation of normalized mean penetration length (x_s/h_j) with α^2. Also plotted are the experimental results of Balachandar et al. (1992) and Tudor (2003). It is evident that the penetration length predicted by the simulation agrees well with the experimental results. Fig. 3.3b shows the variation of the normalized width of the recirculation region (h/h_j) with α^2. Even though the quality trend of the present result is good, there are minor discrepancies in the mean width predicted by the simulation compared to the experimental results. This is attributed, in part, to the uncertainties associated with the measuring technique and the fact that the width of the recirculation region is determined using dye visualization. The diffusing nature of dye results in

26

increased uncertainties due to the enhanced turbulence in CFWJ. In many other studies comparing the geometric width of flow fields, the size as measured by dye (scalar) has been found to be larger than that computed using velocity information (Balachandar et al. 1999). The difference between the experiments of Balachandar et al. (1992), who used a scalar based technique and that of Tudor (2003), who used the velocity profile, further highlights this issue.

Fig. 3.4a shows the normalized mean x-velocity (U/U_j) at several x-locations. It can be seen that the results of the simulations agree well with the experimental results. As Tudor (2003) did not report the turbulence intensity measurements, the present results are compared with the measurements of Tanaka et al. (1994) as shown in Fig. 3.4b at $x/h_j =$ 30 & 40. It is clear that the turbulence intensities predicted by the simulation agrees with the experimental results.

To further validate the results, the normalized axial velocity profile is plotted at various streamwise locations in Fig. 3.5a. Similar to a wall jet, the maximum streamwise velocity (U_m) and jet half-width ($y_{1/2}$) are adopted as the velocity and length scales. From Fig. 3.5a it can be observed that the velocity profiles at locations $x/h_j =$ 40, 45, 50 and 55 nearly collapse onto single curve. However the profiles at $x/h_j =$ 60 begins to deviate from the other profiles and is an indication that the main flow is beginning to influence the wall jet flow. The results are also in accordance with the results of (Mahmoudi and Fleck, 2017), who showed the existence of self-similarity of U for an axial distance of up to 80% of the penetration length for a round CFWJ. The velocity profile of a typical wall jet is also shown in Fig. 3.5a. The jet axial velocity profiles of CFWJ are found to be similar to the wall jet profiles up to $y/y_{1/2} =$ 1.2, i.e., location of

27

inflection point ($\partial^2 U/\partial y^2 = 0$). Above $y/y_{1/2} = 1.2$, there is a difference in the profiles of the CFWJ and the wall jet, due to the effect of the recirculation region. Also, the maximum jet axial velocity occurs at $y/y_{1/2} = 0.2$, which is similar to that reported by (Mahmoudi and Fleck, 2017).

The profiles of the Reynolds shear stress ($-\overline{u'v'}/-\overline{u'v'}_{max}$) are plotted at several streamwise locations in Fig. 3.5b. As expected, the normalized Reynolds shear stress very close to bed is negative. While the velocity profiles appear to collapse on to each other up to $x/h_j = 55$, the Reynolds shear stress profiles do not collapse beyond $x/h_j = 50$. This shows that the fluctuating components of velocity are influenced by the main flow, even if the effects are not apparent in the mean flow components. This further highlights the significance of the turbulence parameters in describing the complex flow features of CFWJ.

3.4   Results and Discussion

3.4.1   Mean Quantities

Fig. 3.6a shows the time-averaged streamwise velocity contours superimposed with the mean velocity vectors in the central plane of the domain. At $x/h_j = 0$, a wall jet emanates into the main flow. The jet gradually loses its momentum as it penetrates the main flow; the region from the jet exit to $x/h_j \approx 10$ resembles the potential-core of a planar wall jet (Rajaratnam, 1976) as shown in the inset of Fig. 3.6a. Beyond this region, the turbulence generated in the shear layer between the jet and the recirculation region, and between the jet and the wall boundary layer penetrates the CFWJ completely. The mean streamwise velocity of the CFWJ becomes zero at the stagnation point. Beyond the location of the stagnation point (SP) the main flow pushes the jet in the opposite direction, forming the

recirculation region, which extends to a height of $y/h_j = 35$. The recirculation region is extended to $x/h_j = 75$ behind the jet exit plane. The locus of $U = 0$ is plotted in Fig. 3.6a which starts from the stagnation point and divides the forward and backward flow. Near the stagnation point as the main flow interacts with the CFWJ, the main flow realigns itself as observed from the vectors in Fig. 3.6a.

Fig. 3.6b shows the mean z-vorticity contours in the central plane. The jet emanates from the nozzle and a high shear region is formed between the CFWJ and the recirculation region above it (red colour marked as SL). As the jet progresses into main flow, the shear layer expands in the vertical direction and the shear layer is turned to generate the recirculation region. The blue colour near the bed shows shear in the wall boundary layer which also expands till the stagnation point is reached. A closer view of the region near the stagnation point is presented in the inset of Fig. 3.6b. The interaction between the main flow and CFWJ results in the formation of vortices near the stagnation point as observed from the velocity vectors in the inset.

Fig. 3.6c shows the contours of RMS values of streamwise velocity fluctuations $\sqrt{\overline{u'^2}}\big/U_j$ in the central plane of the flow field. The maximum value of the turbulence intensity, caused by the interaction of the jet with the main flow and the bed, is observed in the vicinity of the stagnation point (dotted circle). This is consistent with the observations of Tsunoda and Saruta (2003). As expected, the streamwise turbulent intensity is high in the shear layer between the wall jet and the recirculation region. Contours of the normalized mean Reynolds shear stress ($-\overline{u'v'}/U_j^2$) are presented in Fig. 3.6d. The Reynolds shear stress is higher in the regions of greater velocity gradients, i.e.,

29

in the stagnation region and in the shear layer. The jet including the turning flow has a negative shear stress as indicated by the blue colour. The positive peak (indicated by A in the figure, red colour) occurs where oscillatory flow patterns occur, the physical mechanisms of which will be discussed in later sections. Near the stagnation region, the counter-rotating structures from the jet and the main flow interact which causes a positive peak in the Reynolds shear stress(denoted by the letter B).

Fig. 3.7a shows the contours of normalized mean turbulent kinetic energy (TKE$/U_j^2$). As expected, the maximum value of turbulent kinetic energy occurs near the stagnation region i.e., $60 < x/h_j < 75$. The interaction of the CFWJ with the recirculation and with the main flow along the loci of $U = 0$ also causes significant increase in the values of turbulent kinetic energy as observed from Fig. 3.7a. However, from Fig. 3.7a it is apparent the zone of turbulence extends beyond the $U = 0$ line, up to $y/h_j = 50$, thereby making it ideal for mixing applications. Figs. 3.7b and 3.7c show the contours of the flux of the turbulent kinetic energy in the x and y directions given by $F_u = 0.5(\overline{u^3} + \overline{u}\,\overline{v^2} + \overline{u}\,\overline{w^2})$ and $F_v = 0.5(\overline{v^3} + \overline{v}\,\overline{u^2} + \overline{v}\,\overline{w^2})$, respectively. The positive sign of F_u indicates that the flux is in the direction of the CFWJ. Similarly, positive value of F_v in Fig. 3.7c indicates that the flux is in the upward direction and vice versa. From Figs. 3.7b and 3.7c it is apparent that most of the turbulent kinetic energy produced in the stagnation region is transported towards recirculation region where it is dissipated. Since the recirculation region is also in contact with the jet emanating from the nozzle, some of this turbulent kinetic energy would be available to potentially excite the jet. These aspects are discussed in a forthcoming section. The fluxes are maximum near the stagnation region; this is

especially useful in heat transfer applications to achieve higher heat transfer rates from potential hot-spot locations.

3.4.2 Instantaneous Quantities

In order to further evaluate the flow physics responsible for the enhanced turbulence generation in the flow field, the instantaneous flow parameters are analysed. Figs. 3.8a and 3.8b show the instantaneous z-vorticity at time $t = 61$s and 63s, respectively. Counter-rotating vortical structures can be seen emanating from the regions of high shear, i.e., stagnation region, shear layer, boundary layer and along the loci of $U = 0$ (black line in the figures). These structures are mainly responsible for the flux of turbulent kinetic energy which was seen in Fig. 3.7. The structures from the recirculation region interact with the shear layer as shown by black arrow inside the dashed circles (blue color) in Figs. 3.8a and 3.8b. Importantly, one can see a distinct difference in the location of the stagnation point between the two figures. Fig. 3.8a shows the location of stagnation point at $x/h_j = 75$, while in Fig. 3.8b, the location of stagnation point is at $x/h_j = 60$. This highlights the temporal fluctuations of the stagnation point.

The time series of the pressure fluctuations at several near-bed locations close to the stagnation region in the central plane were captured. The Fast Fourier transform (FFT) of pressure data yielded a frequency of 0.3 Hz. The sampling rate for the FFT resolution was 1000 Hz. The corresponding period T for the oscillations was divided into six time steps and the instantaneous streamwise velocity contours at these time instances are presented in Fig. 3.9. Also superimposed in Fig. 3.9 are the instantaneous velocity vectors. As observed in Figs. 3.8a and 3.8b, the vortical structures from the recirculation region interact with the shear layer. The turbulent kinetic energy carried by these vortical

31

structures appear to excite the jet causing instabilities in the shear layer. The jet becomes wavy in nature as observed in the progression of the jet at time $t = T/6$ and 2T/6. The influence of the recirculation region and the adverse pressure gradient the jet encounters enable the detachment from the wall and flap upwards. This allows the main flow to penetrate further into the jet in the near bed region (marked by red arrow inside the dashed circle at $t = T/6$). As the jet flaps back downwards, it collapses the reverse flow region (marked by dashed circle at $t = 2T/6$ & $3T/6$). The interaction of the jet and the reverse flow region generates vortices near the stagnation point ($t = 4T/6$). The wavy nature of the jet continues, and the corresponding main flow adjusts itself to the jet characteristics, reducing the penetration length of the jet. The stagnation point is located at $x/h_j = 55$ as shown by small red arrow at $t = 5T/6$. This phenomenon repeat itself as the penetration length of the jet increases as observed in $t = T$. The jet waviness and the oscillating nature of the stagnation point enhances the mixing. This analysis shows the complex nature of the turbulence in CFWJ flow field and brings forth the feedback mechanism that exists between the recirculation region and the wall jet.

3.4.3 Coherent structures

It is well known that coherent/organized structures are responsible for the transport of mass, momentum and heat transfer in turbulent flows (Wallace, 2009). Since the complete 3D flow field is available from the simulations 'vortex identification techniques' can be used to educe the coherent structures in the flow. The λ_2 criterion is used to identify the coherent structures in the flow. The λ_2 criterion (Jeong and Hussain, 1995) defines a vortex core as a connected region with two negative eigen values of pressure Hessian ($S^2 + \Omega^2$), where S is strain tensor and Ω is rotational tensor, derived by

dropping the unsteady irrotational straining and viscous effects from the Navier Stokes equation. If $\lambda_1, \lambda_2, \lambda_3$ are the eigen values and $\lambda_1 \geq \lambda_2 \geq \lambda_3$, the second largest eigen value should be negative in the vortex core $\lambda_2 < 0$.

Fig. 3.10 shows the coherent structures in the CFWJ flow field captured using λ_2 = -10. The iso-surface (a surface that represents the constant value within the control volume) of λ_2 is colored by the contours of instantaneous z-vorticity, ω_z. Near the stagnation region, the large-scale vortical (tube-like) structures are created by the interaction between the CFWJ, main flow and the bed. As the CFWJ is pushed by the main flow to form the recirculation region, these structures are transported into the recirculation region. During this process and within the recirculation region, these structures interact, and break into the small-scale vortical (worm like) structures as seen in Fig. 3.10. These small-scale structures further interact with the CFWJ giving rise to instabilities i.e., the feedback mechanism. This implies that while most of the turbulent kinetic energy produced at the stagnation point is dissipated in the recirculation region, a portion of the energy is also utilized in exciting the CFWJ emanating from the inlet. It must be noted here that though the λ_2 criterion is one of the most commonly used methods for identifying vortical structures in the flow, the dynamic consideration (pressure minimum) is neither a sufficient nor a necessary condition for the presence of a vortex (Kolar, 2007). In this study, the coherent structures are also quantitatively validated using the turbulent kinetic energy by using the proper orthogonal decomposition.

3.5   Proper Orthogonal Decomposition (POD)

The snapshot approach of POD introduced by (Sirovich et al., 1987) is used in the study. POD is a statistical technique to find the coherent structures using the turbulent kinetic energy criteria. This technique decomposes the fluctuating flow field into a weighted linear sum of eigenfunctions. These eigenfunctions represent the coherent structures present in the flow. The eigenfunction corresponding to the largest eigenvalue represents the most energetic structure. The complete formulation is given in several publications (Meyer et al., 2007 and Jesudhas et al., 2016), and not repeated here for brevity.

Based on the mean flow analysis, the region of interest in the central plane is split into three sections as shown in Fig. 3.11a. The jet region (black color) is chosen to be between $x = 1$ to 1.6 m and $y < 0.1$ m. The recirculation region (red color) extends from $x = 1$ to 2.2 m and $y > 0.1$ m. The stagnation region (blue color) is set between 1.6 to 2.2 and $y < 0.1$. Fig. 3.11b shows the modal energy distribution for the three regions. In the stagnation region, 50% of kinetic energy is recovered in first 5 modes while for the jet and the recirculation regions, the same 50% energy is recovered in 8 and 9 modes, respectively. Also, the first mode contains over 20% of the turbulent kinetic energy in the stagnation region compared to 16% and 14% in the jet and recirculation regions, respectively. This indicates the presence of larger-scale structures in the stagnation region compared to the other two regions.

To quantitatively investigate the contribution of the organized structures to the turbulence statistics, the spatial distribution of the norm, defined by $\sqrt{u'^2 + v'^2}$, for the different modes is first presented considering the complete region of interest (inclusive of

the stagnation, jet and recirculation regions) and is presented in Fig. 3.12. Each mode shows certain characteristics based on how they are projected on the orthogonal basis function. The first mode shows the contribution from the largest structures present in the flow field. The high intensity regions (marked by dashed circles) in the second mode shows the contribution near the stagnation region. In typical turbulent flows, the contribution of higher modes to turbulence quantities is minimal, however, in the CFWJ flow field even the ninth mode makes a significant contribution to the turbulence quantities which shows the dominance of smaller scale structures in the flow. Due to this, the CFWJ is ideal for mixing and heat transfer applications as dissipation occurs at the smaller scales. To further understand the modal distributions in the specific regions of the flow, the jet and stagnation regions are analysed further.

Figs. 3.13a, c, e & g show the spatial distribution of the different modes in the jet region. The high intensity region in mode 1 (Fig. 3.13a) is caused due to the presence of the shear layer between the jet and the re-circulation region. The higher-order modal distributions in Figs. 3.13c, e & g show successive oval patches of high intensity. This is a characteristic signature of a shear layer (Agelin-Chaab and Tachie, 2011; Jesudhas et al., 2016). In a typical wall jet, as the number of mode increases, the modal contribution to the turbulent statistics decreases (Agelin-Chaab and Tachie, 2011). A similar behaviour is observed in the jet region of the present study. Figs. 3.13b, d, f & h depict the spatial distribution of different modes in the stagnation region. The contour for mode 1 depicts the high intensity of turbulence generated in the stagnation region. Similar to the jet region, the contribution of higher-order modes to turbulent kinetic energy decreases. However, from Fig. 3.13h it is evident that the contribution from the ninth

mode to the turbulence statistics is not as significant in the stagnation region as the jet region (Fig. 3.13g).

To extract the coherent structures, the fluctuating flow field is obtained by subtracting the mean from the instantaneous flow field in the stagnation region as shown in Fig. 3.14a. The information about the structures is not evident due to the inclusion of the smaller scales. Reconstruction of the fluctuating flow field is carried out in order to evince the role of the large-scale structures that are present, using a suitable cut-off percentage for the turbulent kinetic energy $tke = \frac{1}{2}(u'^2 + v'^2 + w'^2)$. Figs. 3.14b, c & d show the POD reconstruction based on 20%, 50% and 90% turbulent kinetic energy, respectively. A large-scale (dashed circle in Fig. 3.14b) is educed by filtering out the small-scale structures. This large-scale structure is responsible for the high intensity of turbulence and fluctuations that are generated near the stagnation region. By increasing the cut-off percentage for turbulent kinetic energy, smaller structures are also included in the reconstruction as observed in Fig. 3.14c (dashed circles). Eventually, by including the 100% of turbulent kinetic energy the complete fluctuating flow field will be retrieved. However, from Fig. 3.14d it is apparent that the POD reconstructed field using 90% of turbulent kinetic energy, closely resembles the original fluctuating flow field (Fig. 3.14a). This is because the very small-scale structures contain very little turbulent kinetic energy.

The coherent structures that are responsible for the enhanced turbulence generation in CFWJ flow field are identified using both λ_2 criteria and POD analysis. The results of the POD quantitively validates the results of λ_2 criteria. The results show that the CFWJ flow field is composed of largely small-scale structures. However, the large-scale structures were educed in the stagnation region. These structures were responsible

36

for the high turbulence fluctuations in this region. However, these structures are convected into the recirculation zone, in this process they are immediately broken down into smaller-scales. These small-scale structures are predominantly responsible for the turbulent dissipation (mixing) in CFWJ flow field.
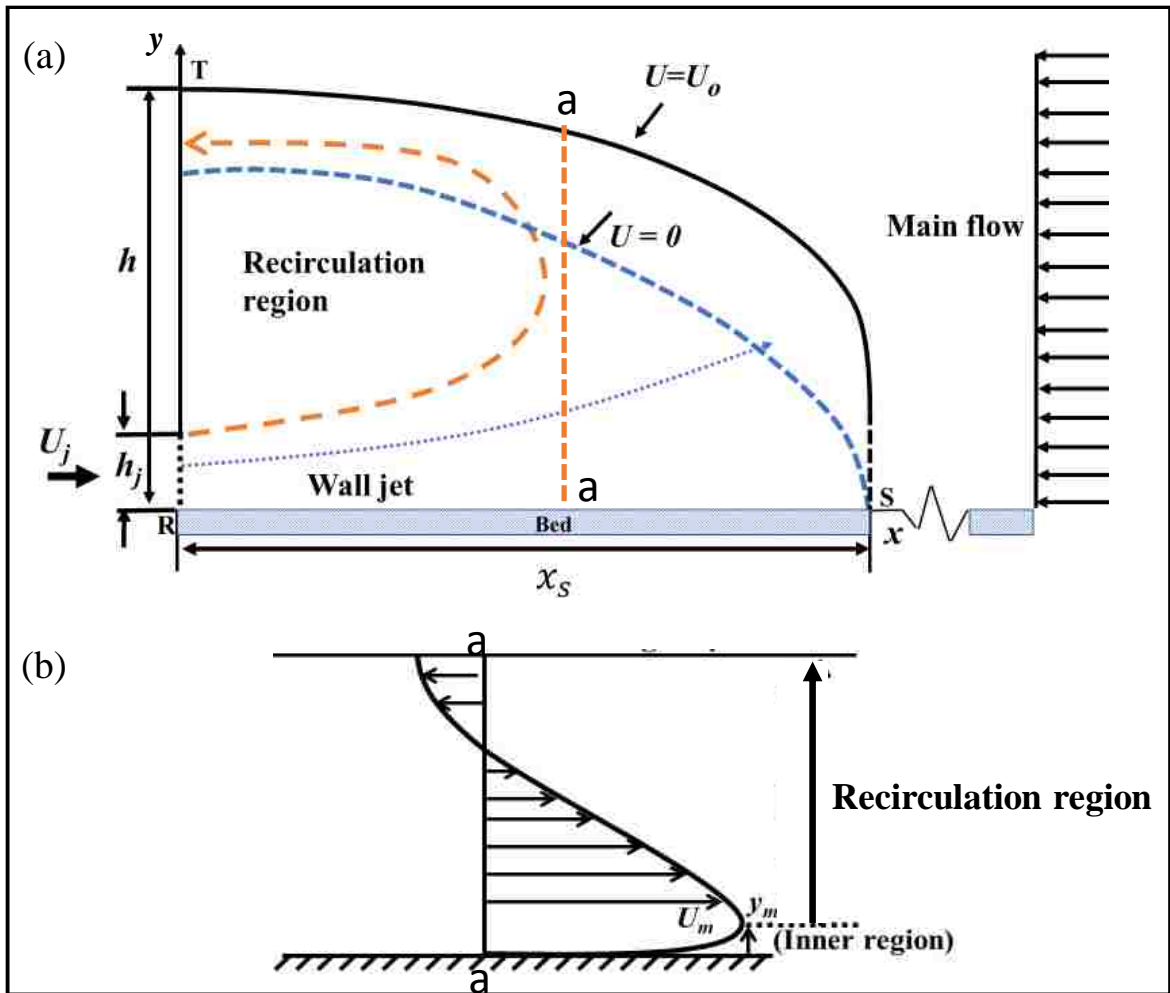
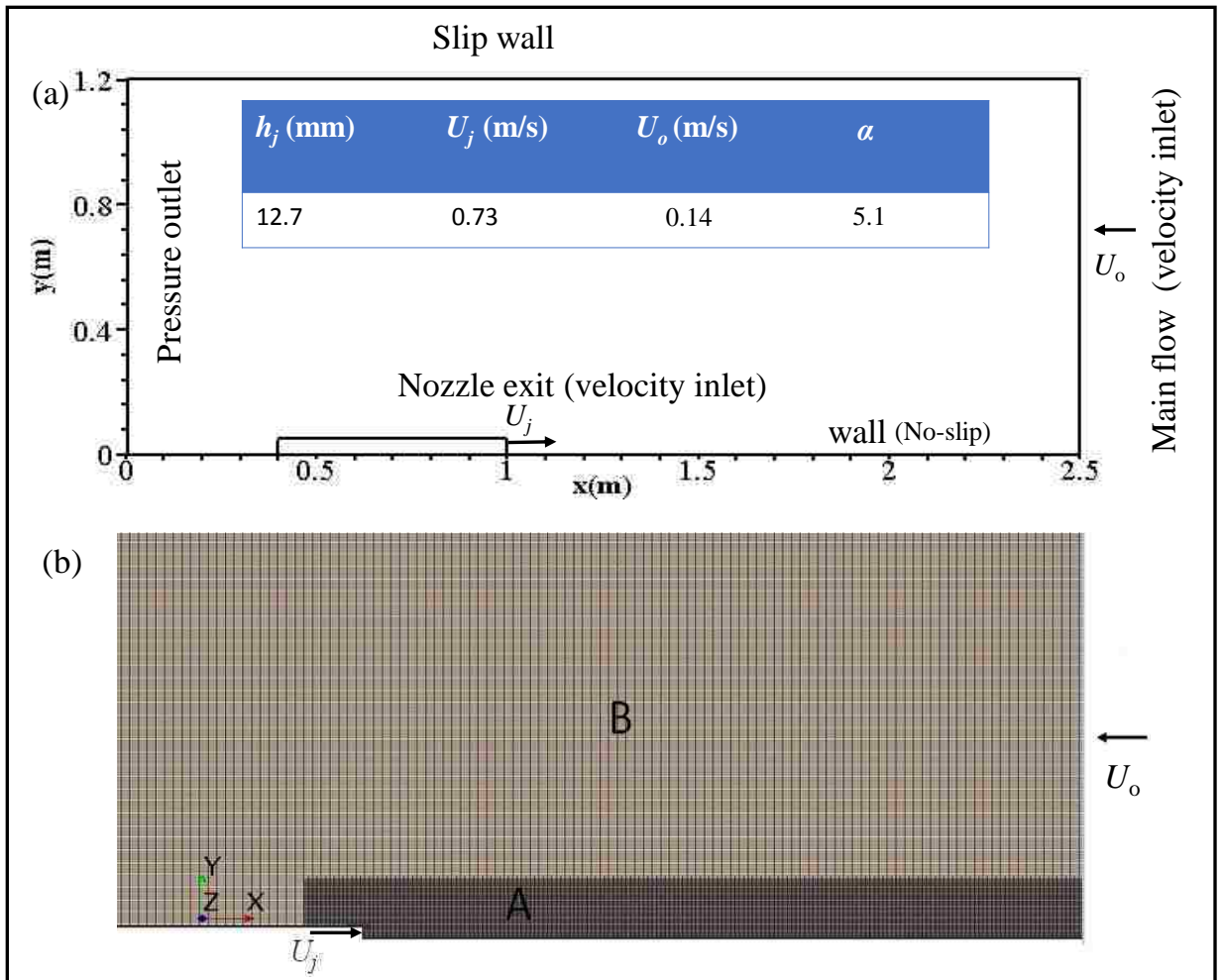Fig. 3.1 (a) Schematic of counter-flowing wall jet (b) velocity profile of CFWJ at section

A-A

h_j (mm)	U_j (m/s)	U_o (m/s)	α
12.7	0.73	0.14	5.1

Fig. 3.2 (a) Computational domain (b) Illustration of computational mesh in the central plane
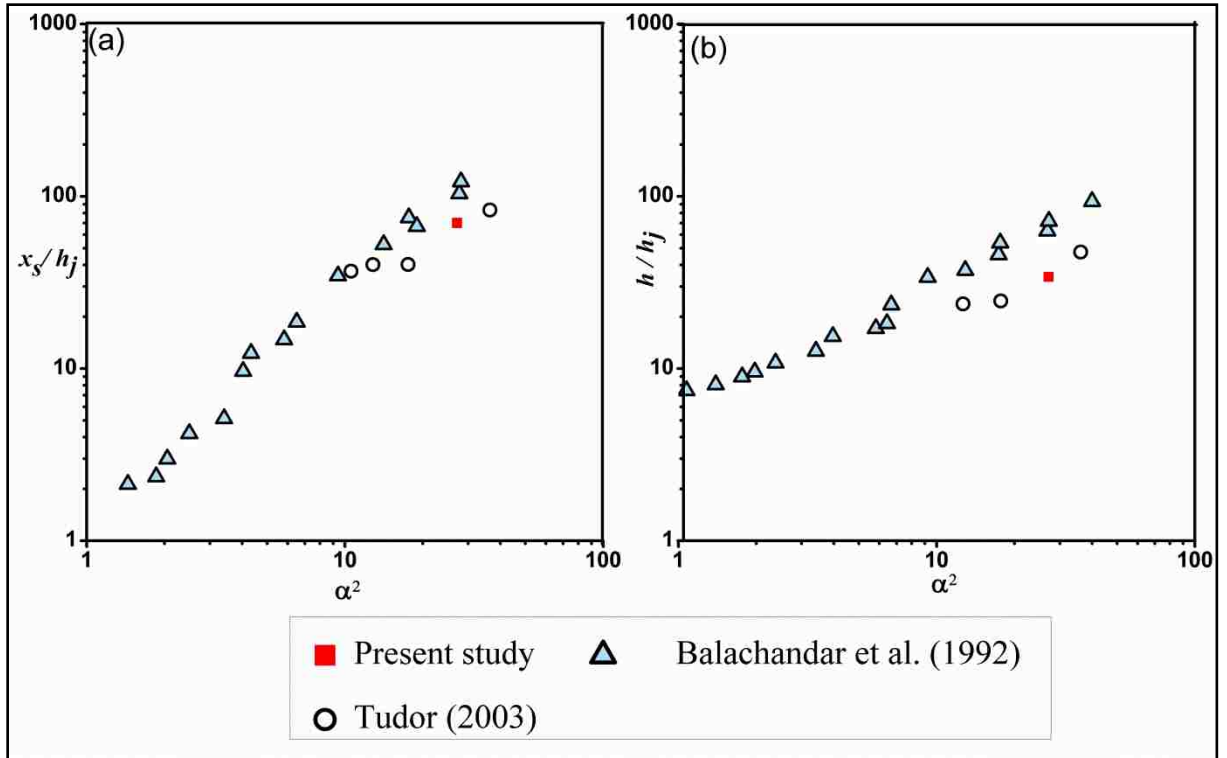
Fig. 3.3 (a) Variation of mean penetration length normalized with the jet size versus α^2

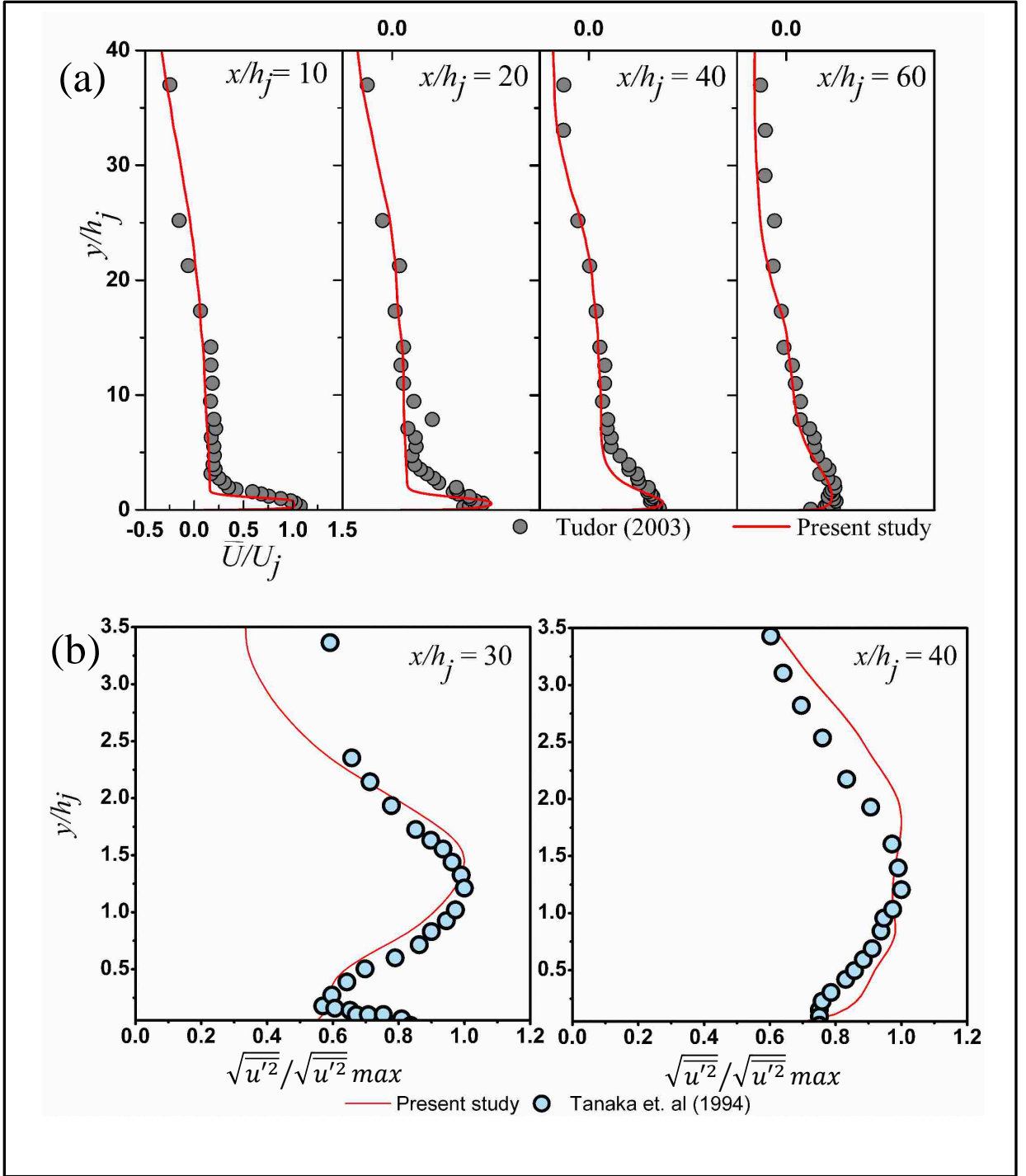(b) Variation of normalized mean width of recirculation region versus α^2

Fig. 3.4 (a) Mean axial velocity ($\overline{U}$) normalized with the nozzle exit velocity at $x/h_j = 10$;

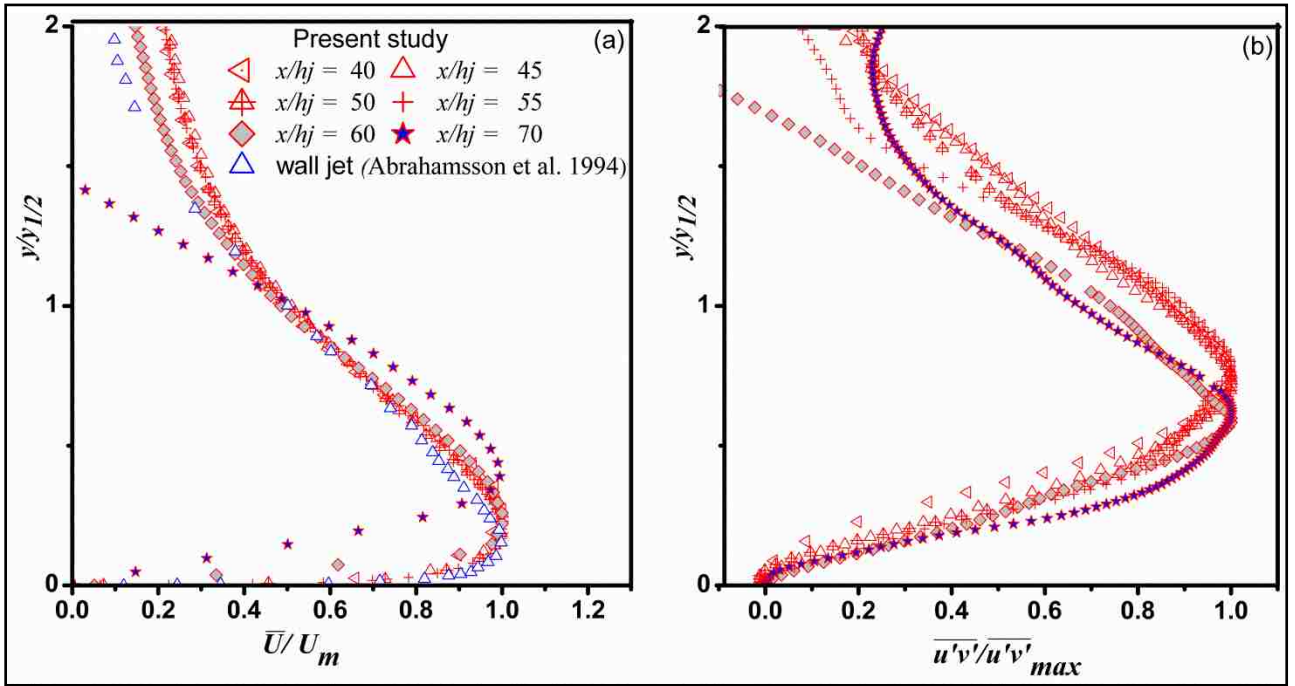$x/h_j = 20$; $x/h_j = 40$; $x/h_j = 60$. (b) Streamwise turbulent intensity at $x/h_j = 30$; $x/h_j =$

40.

Fig. 3.5 (a) Normalized axial velocity profiles of CFWJ (b) Normalized profiles of
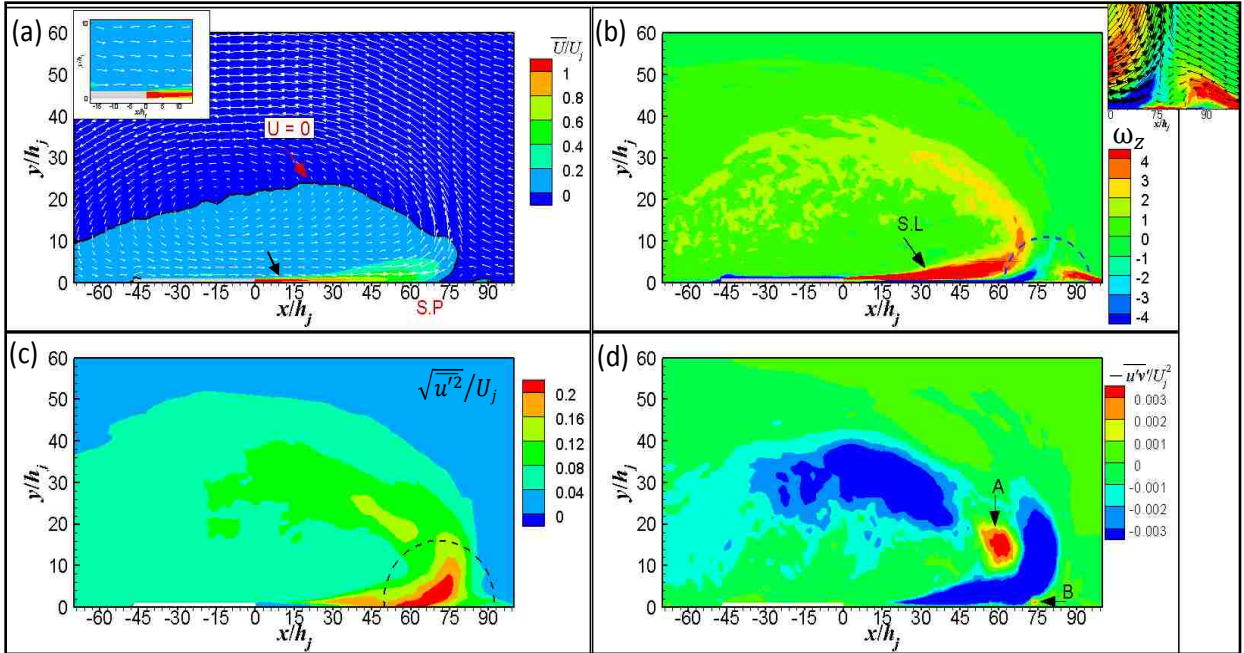
Reynolds stress.

Fig. 3.6 Contours of (a) Mean streamwise velocity (b) Mean z-vorticity (c) Mean

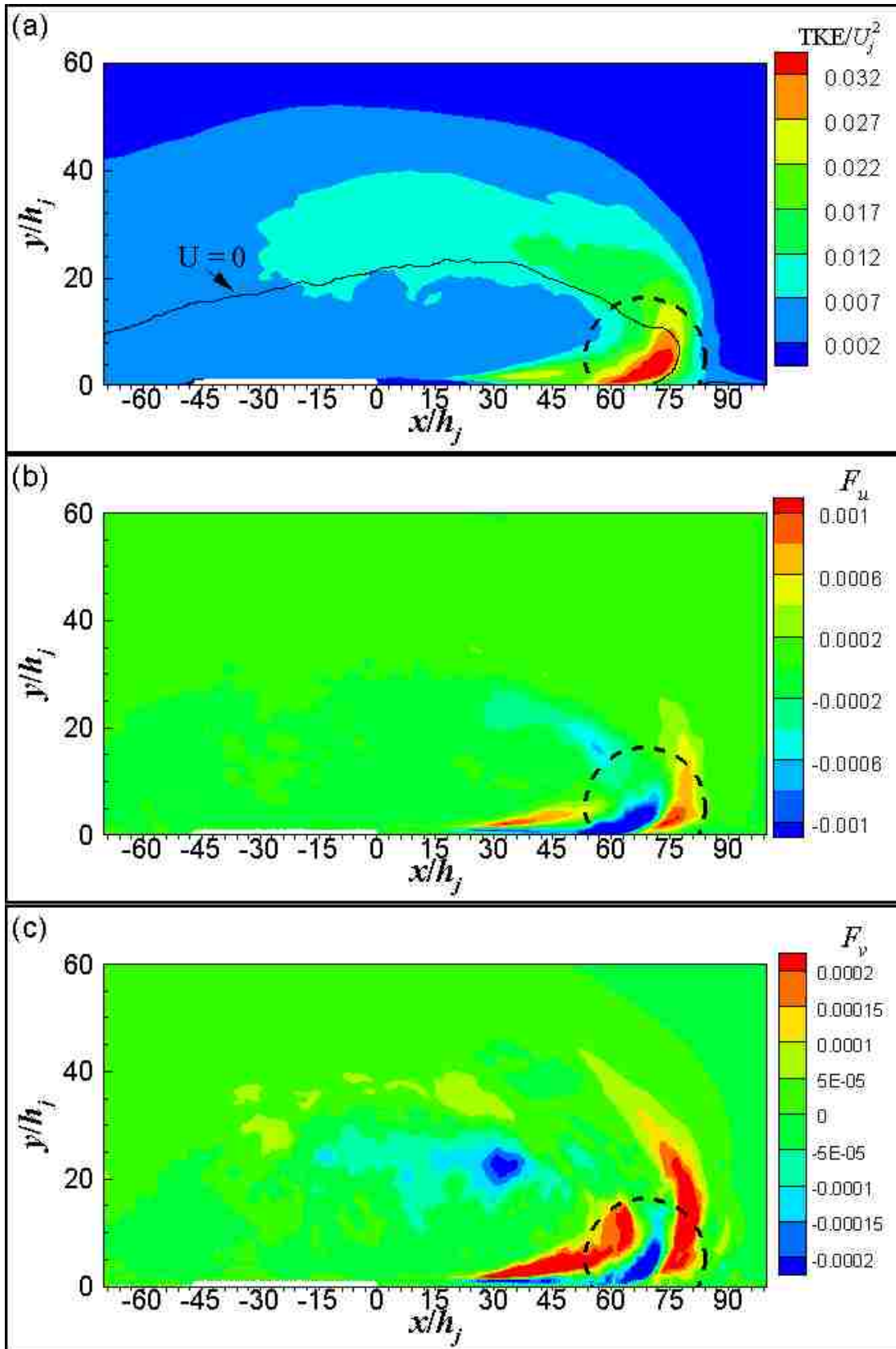streamwise turbulent intensity (d) Mean Reynolds shear stress.

44

Fig. 3.7 (a) Mean turbulent kinetic energy (b) Turbulent flux in x-direction (c) Turbulent
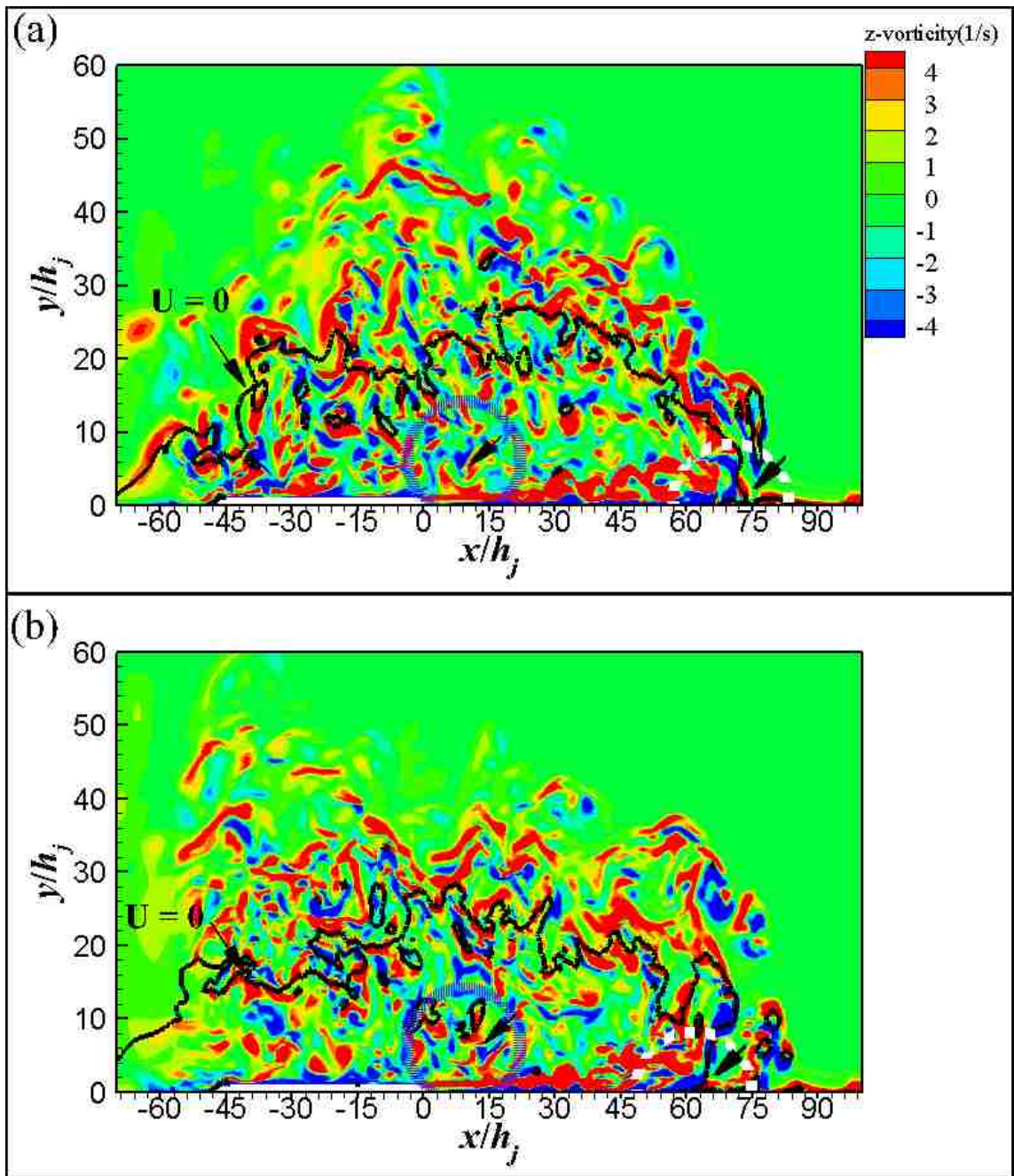
flux in vertical direction

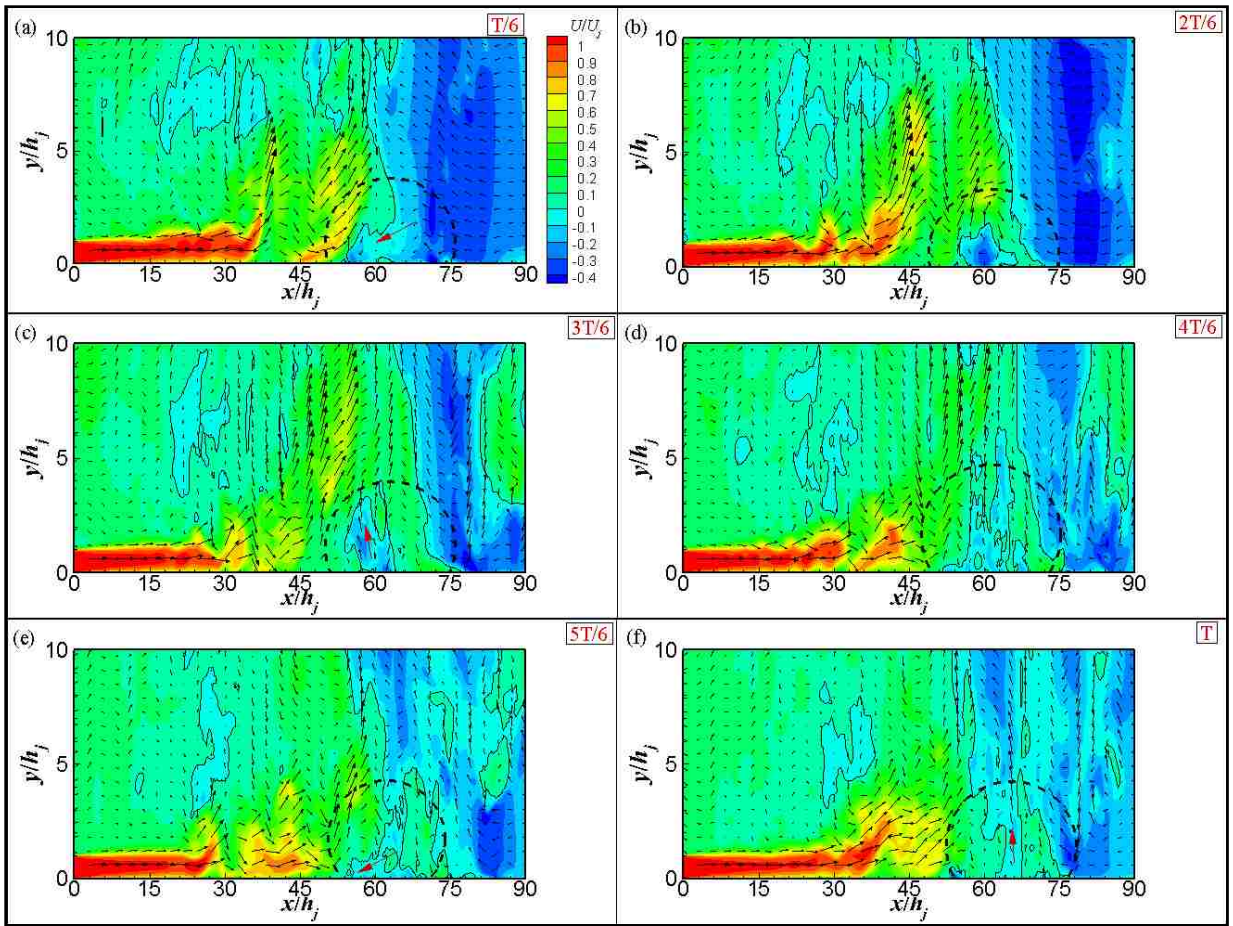Fig. 3.8 Instantaneous z-vorticity at two instants *t* = 61s and 63s

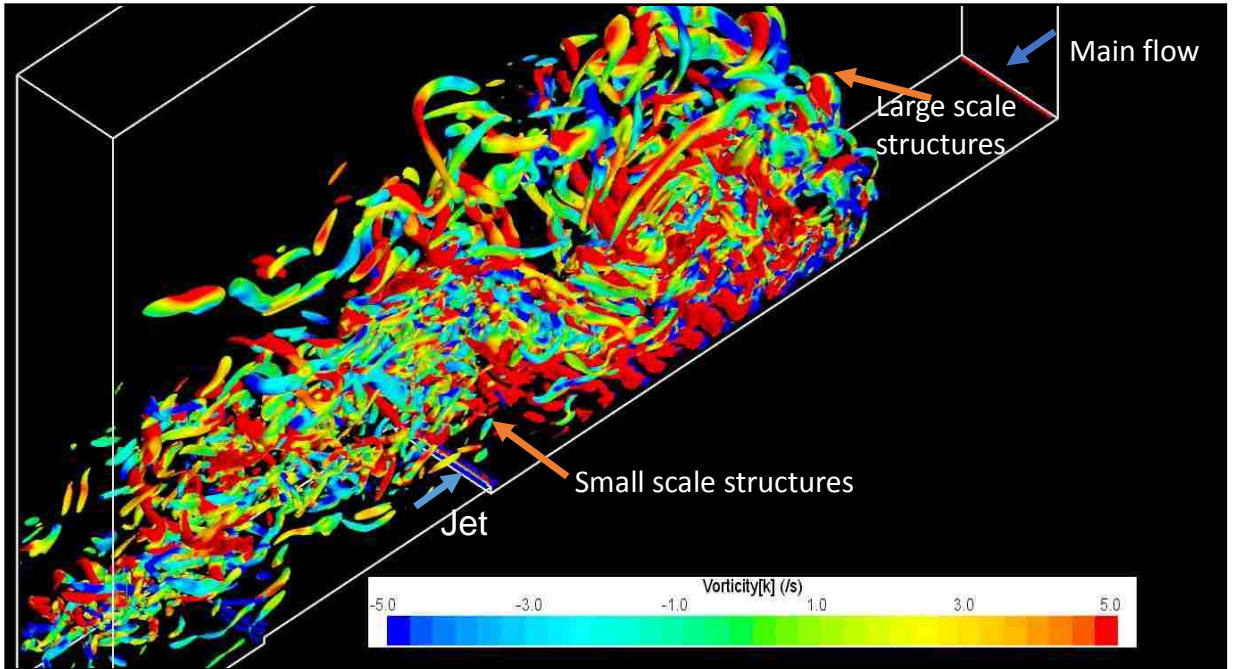Fig. 3.9 Shows the instantaneous streamwise velocity at six instances.

Fig. 3.10 Coherent structures using λ_2 criteria coloured by z-vorticiy
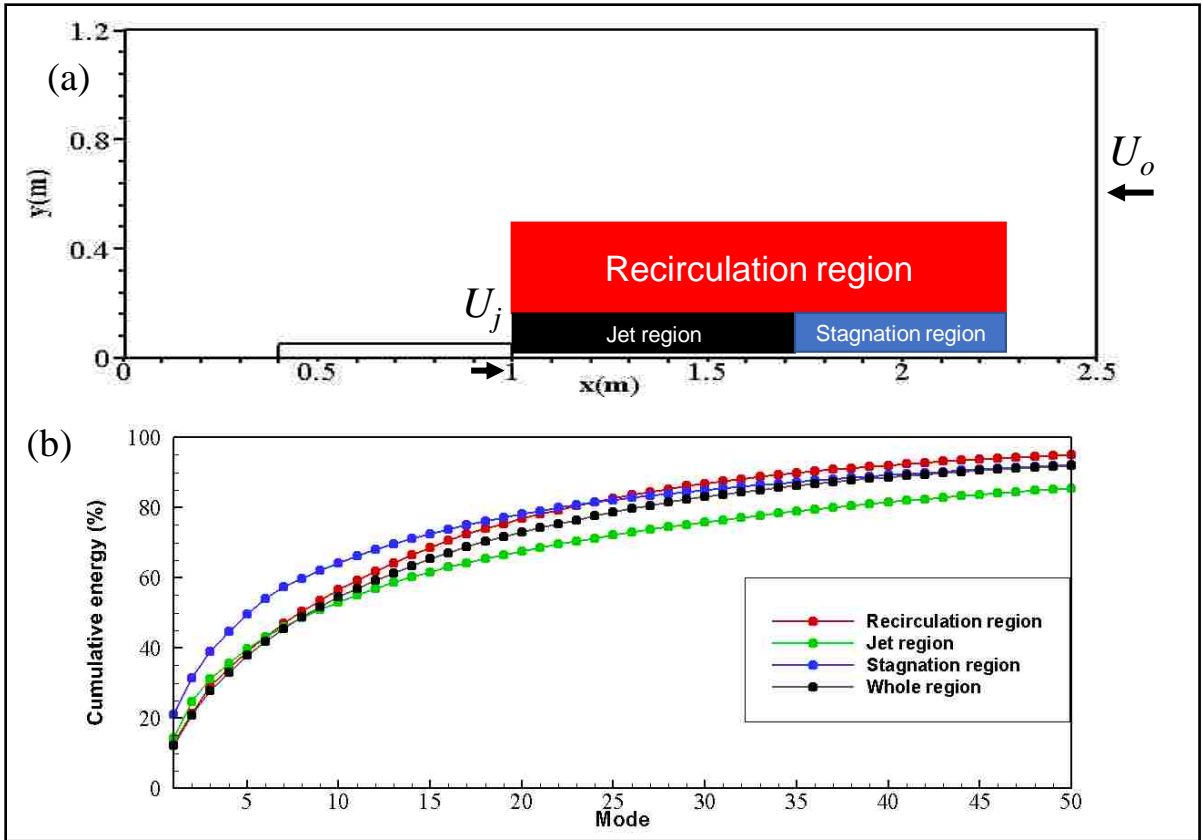
Fig. 3.11 (a) Division of the different regions in the flow field (b) Modal distribution of

the energy in all the regions
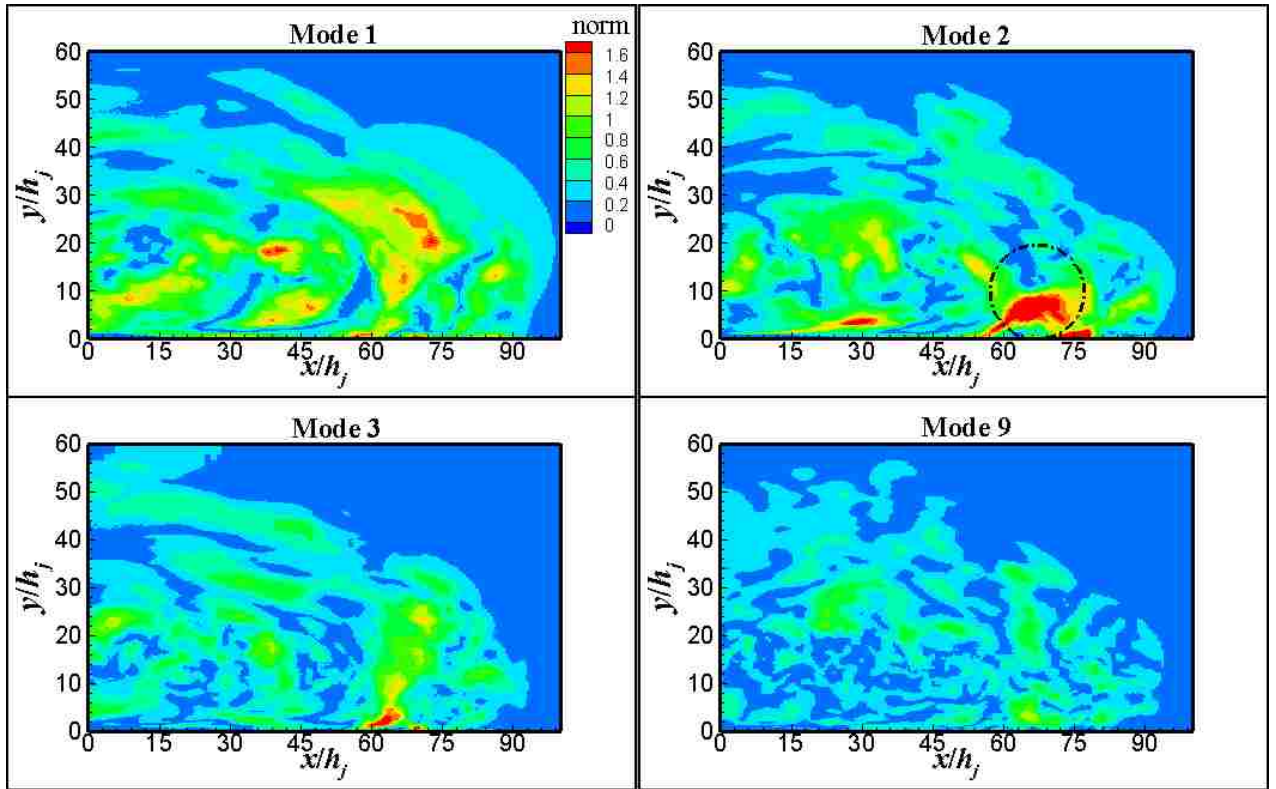
Fig. 3.12 Spatial distribution of norm for different modes considering all three regions:

jet region; stagnation region and recirculation region

Fig. 3.13 (a, c, e, g) Spatial distribution of norm for different modes in jet region (left column) and (b, d, f, h) Spatial distribution of norm for different modes in stagnation region (right column)

Fig. 3.14 (a) Fluctuating component of flow field; (b,c,d) Reconstructing the flow field

based on 20%, 50% and 90% turbulent kinetic energy, respectively

CHAPTER 4. SUMMARY AND CONCULSIONS
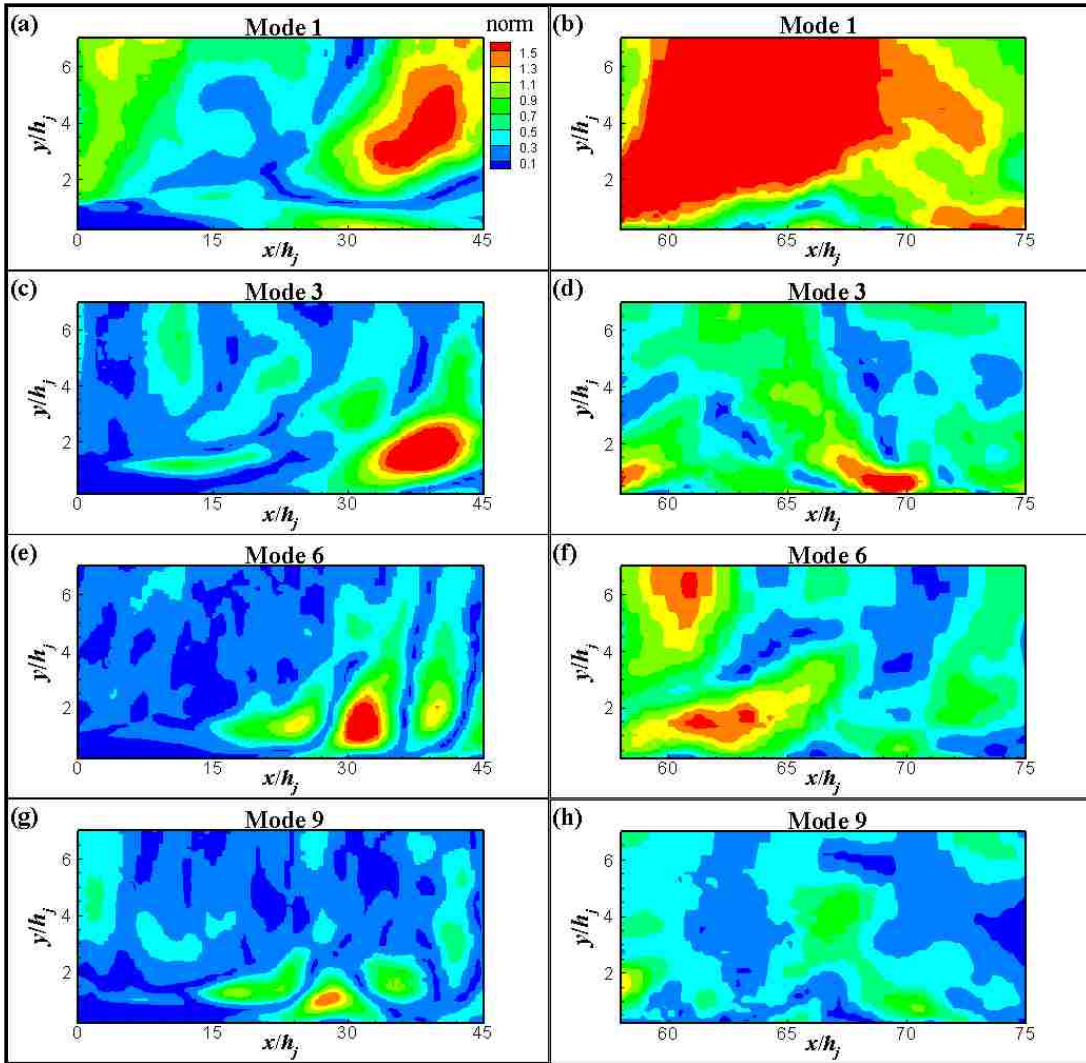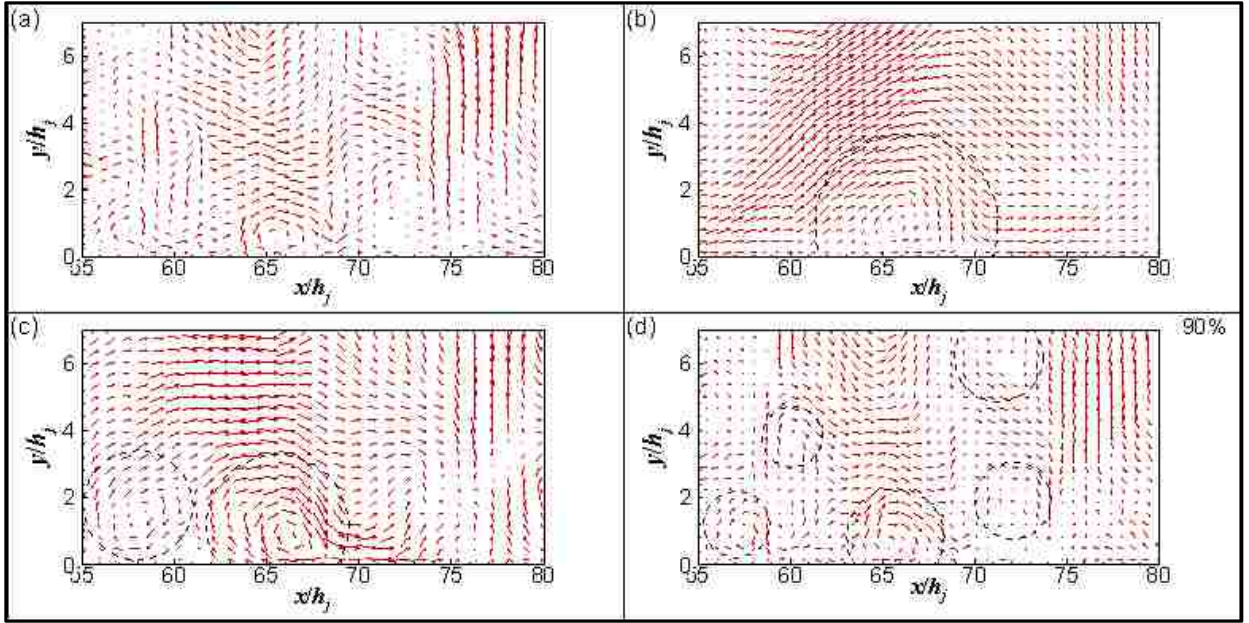
4.1. Summary

The flow field of a counter-flowing wall jet is ideal for mixing because of the presence of the enhanced turbulence. The turbulent structures which are responsible for the enhanced mixing are analyzed in the study. A computational investigation of a counter-flowing wall jet is carried out using 3D, unsteady, Improved Delayed Detached Eddy Simulation.

The simulation result agrees well with the available experimental data. The flow and turbulence characteristics are analyzed by examining the mean and instantaneous quantities. The flow field of the CFWJ is complex and is composed of a variety of fluid structures with different scales which enhances mixing. At the stagnation region, the interaction of jet, the main flow and the near bed turbulence from the wall contributes to a significant level of turbulence. The temporal fluctuations of the stagnation point were accurately captured by the simulation. The feedback mechanism between the recirculation region and the jet region, caused by the transport of vortical structures from the stagnation point to the recirculation zone was found to be responsible for the temporal fluctuations of the stagnation point. These structures are also responsible for inducing a waving nature to the jet emanating from the nozzle.

The coherent structures in the flow were identified using the λ_2 criterion. The large-scale structures from the stagnation region are transported to the recirculation region due to the influence of the main flow. Inside the recirculation region, the large structures are broken into smaller scale structures. Quantitative analysis of the organized structures based on turbulent kinetic energy was carried out using Proper Orthogonal Decomposition (POD). The flow field was divided into three regions to carry out the

POD analysis i.e., the jet region, the stagnation region and the recirculation region. Compared with other turbulent flows, in a CFWJ flow field, the higher-order modes contributed significantly to turbulence, indicating the influence of smaller-scales.

4.2. Future work

The present computation study sheds light on the internal structure of turbulence of a counter-flowing wall jet. Some of the future recommendations are as follows:

- The present simulation is carried out for only value velocity ratio (α). The future work may be extended to include different values of α. The counter-flowing wall jet flow field can be analyzed with heat transfer on the walls.
- Scalar concentration could be included to characterize the mixing characteristics of the counter-flowing wall jet.
- Counter-flowing walls jets are often used in rivers and streams for the mixing of chlorine or other effluents. The effect of free surface deformation on the flow characteristics of the counter-flowing wall jet must be further evaluated.

REFERENCES

Abrahamsson, H., Johansson, B., Lofdahl, L., 1997. Turbulent plane two-dimensional wall-jet in a quiescent surrounding. European Journal of Mechanics13, 533-556

Agelin-Chaab, M., Tachie, M.F., 2011. Characteristics of turbulent three-dimensional wall jets. Journal of Fluids Engineering 133, 0212011-13.

Andreopoulos, J., Rodi, W., 1984. Experimental investigation of jets in a cross-flow. Journal of Fluid Mechanics 138, 93-127

Antonia, R.A., Bilger, R.W., 1974. The prediction of axisymmetric turbulent jet issuing in to a co-flowing stream. The Aeronautical Quarterly 26, 69-80.

Balachandar, R., Robillard, L., Ramamurthy, A.S., 1992. Some characteristics of counter-flowing wall jets. Journal of Fluids Engineering 114, 554-558.

Balachandar, R., Tachie, M.F., Chu, V.H., 1999. Concentration profiles in shallow turbulent sakes. Journal of Fluids Engineering 121, 34-43.

Barata, J.M.M., Ribeiro, S., Santos, P., Silva, A.R.R., 2009. Experimental study of instabilities and secondary effects of a ground vortex flow. Journal of Aircraft 46(4)

Beltaos, S., N. Rajaratnam., 1973. Circular turbulent jet in an opposing infinite stream.Canadian Hydrualics conference, 220-237.

Bernero, S., Fiedler, H.E., 2000. Application of particle image velocimetry and proper orthogonal decomposition to the study of a jet in a counterflow. Experiments in Fluids 29, S274–S281.

Computational Fluid Dynamics Committee (Ed.), 1998. Guide: Guide for the Verification and Validation of Computational Fluid Dynamics Simulations (AIAA G-077-1998(2002)).

Fröhlich, J., von Terzi, D., 2008. Hybrid LES/RANS methods for the simulation of turbulent flows. Progress in Aerospace Sciences 44(5), 349-377.

George, W.K., Abrahamsson, H., Eriksson, J., Karlsson, R.I., LöFdahl, L., Wosnik, M., 2000. A similarity theory for the turbulent plane wall jet without external stream. Journal of Fluid Mechanics 425, 367–411

Hammond, G.P., 1982. Complete velocity profile and "optimum" skin friction formulas for the plane wall-jet. Journal of Fluids Engineering 104, 59-65

Jesudhas, V, 2016. Modelling of Free-surface Flows with Air Entrainment, Ph.D. Dissertation, Univ. of Windsor, Windsor, ON, Canada.

Jeong, J., Hussain, F., 1995. On the identification of a vortex. Journal of Fluid Mechanics 285, 69-94.

Jesudhas, V., Roussinova, V., Balachandar, R., Barron, R., 2016. Submerged hydraulic jump study using DES. Journal of Hydraulic Engineering 143(3), 04016091.

Jesudhas, V., Balachandar, R., Roussinova, V., Barron, R., 2018. Turbulence Characteristics of Classical Hydraulic Jump Using DES. Journal of Hydraulic Engineering 144, 04018022

Kolář, V., 2007. Vortex identification: New requirements and limitations. International Journal of Heat and Fluid Flow 28, 638–652.

Lam, K.M., Chan, H.C., 1995. Investigation of turbulent jets issuing into a counter-flowing stream using digital image processing. Experiments in Fluids 18, 210–212.

Lam, K.M., Chan, H.C., 1997. Round jet in ambient counterflowing stream. Journal of Hydraulic Engineering 123, 895–903.

Launder, B.E., Rodi, W., 1983. The turbulent wall jet measurements and modeling. Annual Review of Fluid Mechanics 15, 429–459

Li, Z., Huai, W., Qian, Z., 2013. Large eddy simulation of a round jet into a counterflow. Science China Technological Sciences 56, 484–491.

Li, Z., Xiao, Y., Tang, H., 2015. Mixing of a non-circular jet into a counterflow. China Ocean Engineering 29, 91–104.

Mahmoudi, M., Fleck, B.A., 2017. Experimental measurement of the velocity field of round wall jet in counterflow. Journal of Hydraulic Engineering 143, 04016076.

Meyer, K.E., Pedersen, J.M., Özcan, O.A., 2007. Turbulent jet in crossflow analysed with proper orthogonal decomposition. Journal of Fluid Mechanics, 583, 199-227.

Menter, F.R., 1992. Improved two-equation k-omega turbulence models for aerodynamic flows. AIAA Journal 6, 1657-1659.

Morgan, W.D., Brinkworth, B.J., Evans, G.V., 1976. Upstream penetration of an enclosed counter-flowing jet. Industrial & Engineering Chemistry Fundamentals 15, 125–127.

Nasif, G., Barron, R.M., Balachandar, R., 2014. DES evaluation of near-wake characteristics in a shallow flow. Journal of Fluids and Structures 45, 153–163.

Peck, R.E., 1981. Aerodynamics of a round jet in a counter-flowing wind. Journal of Aircraft 18, 61-62.

Rajaratnam, N., 1976. Turbulent jets. Developments in Water Science, 5, 211-224.

Shur, M.L., Spalart, P.R., Strelets, M.K., Travin, A.K., 2008. A hybrid RANS-LES approach with delayed-DES and wall-modelled LES capabilities. International Journal of Heat and Fluid Flow 29, 1638–1649.

Sirovich, L., 1987. Turbulence and the dynamics of coherent structures. Part I: Coherent structures. Quarterly of Applied Math., XLV(3), 561-571.

Sivapragasam, M., Ramamurthy, S., Deshpande, M.D., Sridhara, S.M., 2009. Computation of turbulent jets in annular counter flow. Centre of fluid flow and energy system research, 11th Annual CFD Symposium,1-8,Banglore

Spalart, P. R., Jou, W. H., Strelets, M., Allmaras, S. R.,1997. Comments on the feasibility of LES for wings, and on a hybrid RANS/LES approach. Advances in DNS/LES, 1, 4–8.

STAR-CCM, User Guide, (2013). Version 10.06. 010.

Tachie, M., Balachandar, R., Bergstrom, D., 2002. Scaling the inner region of turbulent plane wall jets. Experiments in Fluids 33, 351–354

Tanaka, E., Inoue, Y., Yamashita, S., 1994. An experimental study on the two-dimensional opposed wall jet in a turbulent boundary layer: Change in the flow pattern with velocity ratio. Experiments in Fluids 17, 238–245.

Tsunoda, H., Saruta, M., 2003. Planar laser-induced fluorescence study on the diffusion field of a round jet in a uniform counter-flow. Journal of Turbulence 4,1-12.

Tudor, M., 2003. Turbulent Characteristics of a Counter Flowing Wall Jets, Master's Thesis, Concordia University, Montreal, QC, Canada.

Versteeg, H.K., Malalasekera, W., 2007. An Introduction to Computational Fluid Dynamics: The Finite Volume Method, 2nd ed., Pearson Education Ltd, Harlow, England; New York.

Volchkov, E.P., Lebedev, V.P., Nizovtsev, M.I., Terekhov, V.I., 1995. Heat transfer in a channel with a counter-current wall jet injection. International Journal of Heat and Mass Transfer 38, 2677–2687.

Wallace. J.M., 2009. Twenty years of experimental and direct numerical simulation access to the velocity gradient tensor: What have we learned about turbulence? Physics of Fluids, 21(2), 021301.

Yoda, M., Fiedler, H.E., 1996. The round jet in a uniform counterflow: flow visualization and mean concentration measurements. Experiments in Fluids 21, 427–436.

VITA AUCTORIS

NAME: Sachin Sharma

PLACE OF BIRTH: Sonepat, Haryana, India

YEAR OF BIRTH: 1988

EDUCATION: S.D.M, School, 2006

                         National Institute of Technology, Kurukshetra,
                         India, 2013

                         University of Windsor, MASc., Windsor, ON,
                         2018